Cohesive - frictional crack model applied to bi-material interfaces

Andrea Alberto

Cohesive - frictional crack model applied to bi-material interfaces

Tesi per il conseguimento del titolo di Dottore di Ricerca
XXV Ciclo (2010-2011-2012)

Dottorato di Ricerca in Ingegneria delle Strutture
Politecnico di Torino

Febbraio 2013

Dottorato di Ricerca in Ingegneria delle Strutture
Politecnico di Torino, Corso Duca degli Abruzzi 24, 10129 Torino, Italy

Tutore: Prof. Silvio Valente

Settore Scientifico-Disciplinare: ICAR/08 - Scienza delle Costruzioni

Coordinatore: Prof. Alberto Carpinteri

Summary

The necessity of ensuring conditions of reliability and safety for constructions in both civil and infrastructural fields, have led more and more to the development of numerical methods that are able to simulate the behavior of cracked materials, wherever a comparison with laboratory tests is not possible because of the size of the works. Given the importance of cracking phenomena in quasi-brittle materials, such as concrete, rocks and bricks, and considering the importance of fully understanding brittle type collapses, it would seem useful to develop numerical procedures that are able to supply correct predictions of the behaviour of a structure. In the first part of the thesis, starting from considerations made on homogeneous material , a method has been developed on the basis of the asymptotic development of a crack that propagates at the interface of two generic materials. Then, referring to the foundations of a dam , this method has been applied to an interface between Rock and Concrete, and a comparison has been made between the acquired results and those obtained using a Finite Element Method. In the second part of the thesis, the mechanical behaviour of the interface between Mortar and Brick and Mortar and Stone has been analyzed through the use of a cohesive model, as part of the REFRESCOS project. Numerical simulation of laboratory tests has described the detachment phenomenon between the two materials in a satisfactory manner. This simulation can be used to predict such a phenomenon, that is frequently encountered in plasterwork in historical brickwork constructions.

Acknowledgments

I would sincerely like to thank Professor Silvio Valente, my tutor, for the passion and dedication with which he has transmitted determined topics, thus allowing me to grow, from the scientific point of view, during my doctorate studies. Warm thanks are also due to Professor Alberto Carpinteri, Coordinator of the Research Doctorate studies, for the lessons he has conveyed during this period of study. Special thanks go to my wife, Stefania, for the commitment she has shown in supporting my choices, my brother Massimo,Gabriele my faithful colleague of study, my mother Antonella and my father Claudio, for their constant presence, and last but not least, my grandmother Tere for having transmitted the humility necessary to face everyday events.

Ringraziamenti

Desidero sentitamente ringraziare il Prof.Silvio Valente,tutore, per la passione e dedizione, con cui mi ha trasmesso determinati argomenti permettendomi di crescere nella mia formazione scientifica nel corso del dottorato, il Prof. Alberto Carpinteri, Coordinatore del Dottorato di Ricerca, per gli insegnamenti che mi ha impartito nel corso di questo periodo di studio. Un ringraziamento speciale va a mia moglie Stefania per l'impegno dimostrato nell'assecondarmi nelle mie scelte, mio *fratello* Massimo,Gabriele mio fedele Collega di studio e Lorenzo, Mamma Antonella, Papá Claudio per la loro presenza costante e Nonna Tere per l'avermi trasmesso l'umiltá necessaria per affrontare i quotidiani avvenimenti. Un particolare ringraziamento va alla mia seconda famiglia Marilena,Pier, Francesca, Simone e le due meraviglie Diego e Anita per essere magicamente loro stessi.

Contents

Chapter 1

Elements pertaining to Fracture Mechanics

1.1 Introduction

Applications of fracture mechanics to concrete have been going on since the early sixties.Linear elastic fracture mechanics models were the only available models which treated crack stability and crack growth in concrete until the mid-seventies when models based on cohesive zone started to be used.During the eighties the major fracture mechanics research activities on cohesive zone model were aimed at further development of tensile-softening model,determination of the requisite material properties and applications of the models to structures with various geometry and size. It has been demonstrated, see [1],[2], [3] that propagation of a real crack in cementitious materials is preceded by formation of a fracture process zone that governs the structural behaviour of concrete. Furthermore, it has been demonstrated that the effects of fracture process zone cannot be omitted from the mechanical analysis as far as structures of medium or large size are concerned. Fracture mechanics is that part of continuum mechanics that deals with the behaviour of cracked solids. The basis of this subject

is the study of the concentrations of the stresses at the crack tip in a remote stressed slabs. The concepts of stress intensity factor and plastic zone can to explain the phenomenon of the transition from ductile to brittle behaviour of samples of various shapes with geometrical ratios that remain constant as the size grows (scale effect on apparent strength of materials).

1.2 Concentration of the stresses

The presence of a circular opening in a uniformly stressed slab leads to an increase in the stress value on the border of the opening itself which is equal to three times the value of stress σ applied at an infinite distance [4] as shown in Figure 1.1 (a). In this case, the stress intensity factores is equal to 3. In the case of an elliptic opening, with semi-axes a and b, the stress in correspondence to the edge of the opening is equal to $1 + 2\ a/b$ times the value of the stress applied at an infinite distance [5], and the intensification factor therefore results to be $1 + 2\ a/b$, as shown in Figure 1.1 (b). The strength of the slab therefore depends on the relationship between the a and b semi-axes of the elliptic opening. In the case of a very elongated ellipse (to which a crack can be assimilated), the stress intensity factores tends to ∞, and originates such a stress value that it exceeds the ultimate tensile strength σ_p, even for very low extreme stress values σ, as in 1.1 (c).

This leads to the conclusion that cracked slabs have no tensile strength, a conclusion that is in contrast with what has actually been observed. In order to overcome this problem, Griffith [6] and [7] proposed an energy type approach. According to Griffith, the elastic deformation energy W_e released from a uniformly stressed slab of unitary thickness, is proportional to the energy contained within the circle of the radius before a crack of length $2a$ develops:

$$W_e = \pi a^2\ \frac{\sigma^2}{E} \tag{1.1}$$

where E represents the elastic modulus of the material that makes up

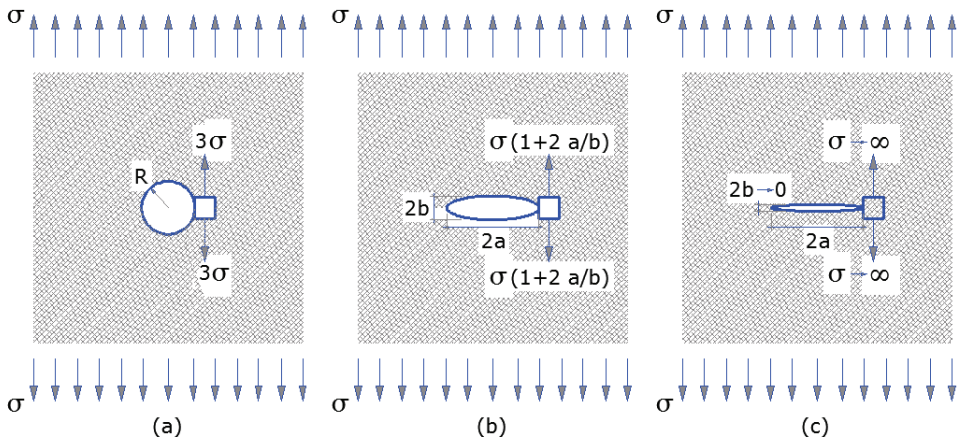

Figure 1.1. Stress states in perforated slabs. (a) circular opening, (b) elliptic opening, (c) crack

the slab. The previous relation is valid in the case in which the displacements at the infinity of the slab are kept constant. In order to create a crack of length $2a$, it is necessary to have a surface energy equal to:

$$W_s = 4\ a\ \gamma \tag{1.2}$$

in which γ represents the energy per surface unit. The condition necessary to obtain an extension of the crack is:

$$\frac{d\ W_e}{da} > \frac{d\ W_s}{da} \tag{1.3}$$

which leads to the instability condition:

$$2\pi\ a\frac{\sigma^2}{E} \geq 4\ \gamma \tag{1.4}$$

and obtaining σ, it is possible to obtain

$$\sigma \geq \sqrt{\frac{2\gamma\ E}{\pi\ a}} \tag{1.5}$$

or

$$\sigma \geq \sqrt{\frac{\mathcal{G}_{IC}\ E}{\pi\ a}} \tag{1.6}$$

where $\mathcal{G}_{IC}$ represent the Fracture Energy.

The Figure 1.2 shown the stress σ in function of the semi-length of the crack:

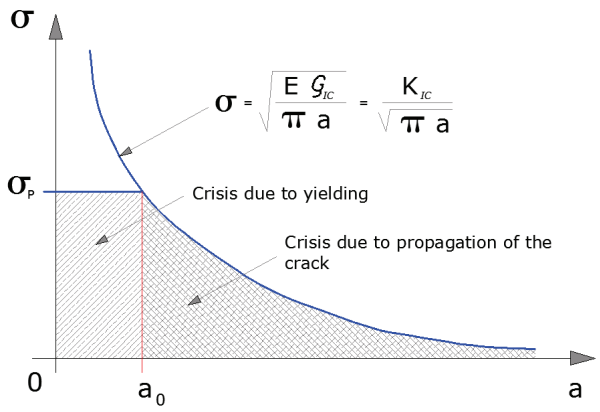

Figure 1.2. Stress in function of the semi-length of the crack

It can be noticed that for a tending to infinity, the strength of the slab correctly tends to zero, while for a tending to zero, the strength tends to reach infinite values. The latter result is not coherent with the existence of a yielding limit σ_p of the slab. It is therefore necessary to limit the previous diagram to values of $\sigma \leq \sigma_p$, by introducing the equivalent length of the micro-crack $2a_0$ [8]:

$$a_0 = \frac{\mathcal{G}_{IC}E}{\pi\sigma_p^2} \tag{1.7}$$

where, below a_0 , the yielding precedes the propagation of the crack (which is not necessarily unstable, as can be seen at the end of the chapter).

1.3 Linear elastic fracture mechanics

As an alternative to the energy-type theory proposed by Griffith, it is possible to study the stability conditions of a crack on the basis of considerations on the elastic stress state in the zone close to the apex of the crack. There are three elementary crack opening modes:

- Opening (Mode I)
- Sliding on the plain (Mode II)
- Shear outside the plain (Mode III)

highlighted in the picture below:

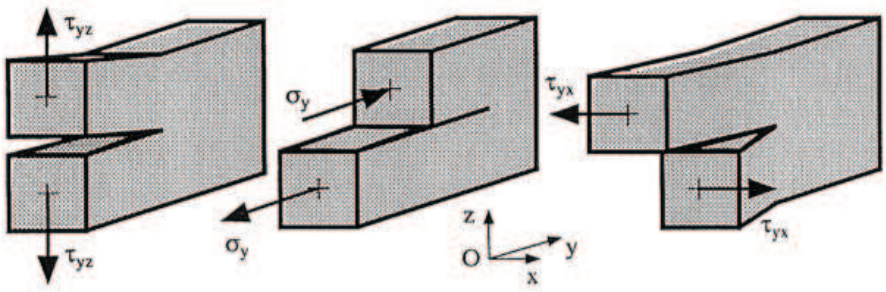

Figure 1.3. Crack opening modes. (a) Mode I, (b) Mode II, (c) Mode III

The stress state at the apex of the crack was calculated by Irwin [9], adopting the method proposed by Westergard [10], on the basis of the stress intensity factores.

In the case of Mode I, one obtains:

$$\begin{Bmatrix} \sigma_x \\ \sigma_y \\ \tau_{xy} \end{Bmatrix} = \frac{K_I}{\sqrt{2\pi r}} \begin{Bmatrix} \cos\frac{\vartheta}{2}\left(1 - \sin\frac{\vartheta}{2}\sin\frac{3\vartheta}{2}\right) \\ \cos\frac{\vartheta}{2}\left(1 + \sin\frac{\vartheta}{2}\sin\frac{3\vartheta}{2}\right) \\ \sin\frac{\vartheta}{2}\cos\frac{\vartheta}{2}\cos\frac{3\vartheta}{2} \end{Bmatrix}$$

In the case of Mode II:

$$\begin{Bmatrix} \sigma_x \\ \sigma_y \\ \tau_{xy} \end{Bmatrix} = \frac{K_{II}}{\sqrt{2\pi r}} \begin{Bmatrix} -\sin\frac{\vartheta}{2}\left(2+\cos\frac{\vartheta}{2}\cos\frac{3\vartheta}{2}\right) \\ \cos\frac{\vartheta}{2}\sin\frac{\vartheta}{2}\cos\frac{3\vartheta}{2} \\ \cos\frac{\vartheta}{2}\left(1-\sin\frac{\vartheta}{2}\sin\frac{3\vartheta}{2}\right) \end{Bmatrix}$$

and, finally, for Mode III:

$$\begin{Bmatrix} \tau_{xz} \\ \tau_{yz} \end{Bmatrix} = \frac{K_{III}}{\sqrt{2\pi r}} \begin{Bmatrix} \sin\frac{\vartheta}{2} \\ \cos\frac{\vartheta}{2} \end{Bmatrix}$$

In the previous formulas, r represents the radial distance from the extremity of the crack and "θ" is the angle with respect to the x axis that can be observed in Figure 1.4:

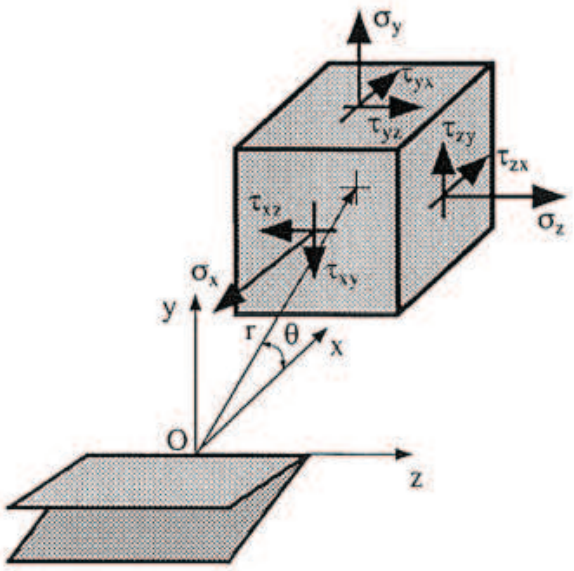

Figure 1.4. Global stress state

and K_I,K_{II},K_{III} are the three intensification factors of the stresses which are defined as follows:

$$\mathbf{K} = \left\{ \begin{array}{c} K_I \\ K_{II} \\ K_{III} \end{array} \right\} = \lim_{r \to 0} \left\{ \begin{array}{l} \left| \sqrt{2\pi r}\sigma_y \right|_{\vartheta=0} \\ \left| \sqrt{2\pi r}\tau_{xy} \right|_{\vartheta=0} \\ \left| \sqrt{2\pi r}\tau_{yz} \right|_{\vartheta=0} \end{array} \right\}$$

It should be pointed out that the stress components and the angular profile of the stress field show a singularity at the edge of the crack of the type $r^{-1/2}$, which only depends on the boundary conditions on the crack faces and not on the infinite conditions. The stress field around the edge of the crack is univocally determined by K_I,K_{II},K_{III}. The latter depend on the geometry, the length of the crack and on the loading conditions.

The unusual physical dimensions of K_I,K_{II},K_{III} $[F][L]^{-3/2}$ are responsible for the scale effects in crack mechanics and therefore in the apparent strength of materials. Values of K_I,K_{II},K_{III} can be found in the manuals written by Sih [11], Tada, Paris and Irwin [12], Rooke and Cartwright [13] and Murakami [14] for different geometries, cracks and loading conditions. Figure 4.5 shows, as an example, the cases of bi-axial traction (Mode I) and shear stresses (Mode II):

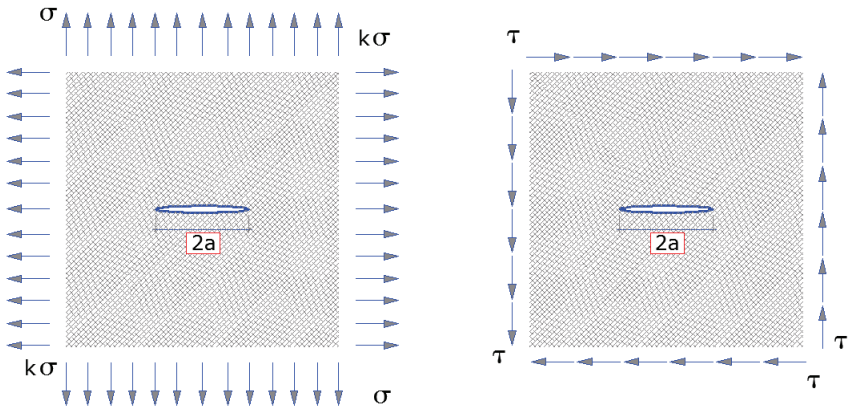

Figure 1.5. Examples of stress intensity factors

in which the stress intensity factors are equal to:

$$K_I = \sigma\sqrt{\pi a} \quad e \quad K_{II} = \tau\sqrt{\pi a}$$

Any stress state can be obtained as a linear combination of the stress states relative to the Mode I, Mode II and Mode III cases. Introducing the five stress components $\sigma = \{\sigma_n,\sigma_b,\tau_{nb},\tau_{nt},\tau_{tb}\}$, it is possible to express the stress state as follows [15]:

$$\sigma = (2\pi r)^{-1/2}\mathbf{F}(\vartheta,\varphi)\mathbf{K}$$

in which $\mathbf{F}(\vartheta,\varphi)$ indicates the matrix, of dimensions 5x3, of the angular profile of the stress state that is a function of the latitude θ and longitude φ measured in the local reference t,n,b defined in Figure 1.6.

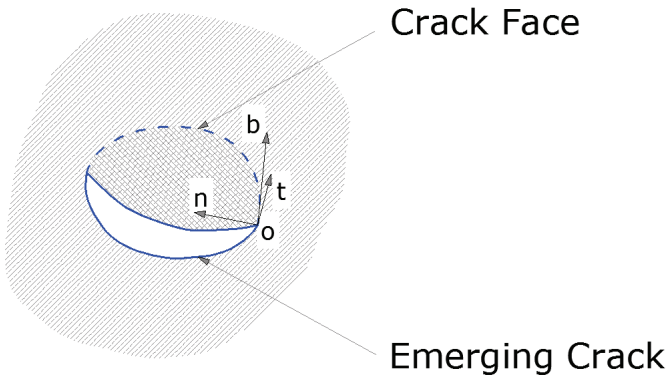

Figure 1.6. Lopsided crack with the local reference t,n,b.

1.3.1 Crack propagation conditions

According to Griffith, the unstable propagation of a crack begins when the rate of energy released by crack $\mathcal{G}$ exceeds the energy necessary to create a new portion of crack $\mathcal{G}_{IC}$, which is known as the critical rate of release of deformation energy ([6] and [7])

Therefore, in the case of Mode I:

$$\mathcal{G}_I = \mathcal{G}_{IC}$$

In Linear Elastic Fracture Mechanics, the stress field close to the apex of the crack is univocally defined by the vector K. For this reason, it is assumed that the propagation of the crack begins when K reaches its critical value K_c, which is known as toughness. Vector K, containing the three values K_I, K_{II} e K_{III} , can be compared with the vector $\mathcal{G}$, containing the three fracture energy values $\mathcal{G}_I$ $\mathcal{G}_{II}$ e $\mathcal{G}_{III}$:

$$\mathcal{G} = \begin{Bmatrix} \mathcal{G}_I \\ \mathcal{G}_{II} \\ \mathcal{G}_{III} \end{Bmatrix} = \begin{Bmatrix} \frac{K_I^2}{E'} \\ \frac{K_{II}^2}{E'} \\ \frac{K_{III}^2}{\mu} \end{Bmatrix}$$

where $E' = E$ in the case of a plain stress state and $E' = E(1 - \nu^2)$ in the case of a plain strain state. The Poisson coefficient is therefore indicated with ν and the transversal elastic modulus is indicated with $\mu = E/(2(1 + \nu))$.

A similar relationship can be written when the stresses achieve the critical values: K_{IC} e $\mathcal{G}_{IC}$:

$$\mathcal{G} = \begin{Bmatrix} \mathcal{G}_{IC} \\ \mathcal{G}_{IIC} \\ \mathcal{G}_{IIIC} \end{Bmatrix} = \begin{Bmatrix} \frac{K_{IC}^2}{E'} \\ \frac{K_{IIC}^2}{E'} \\ \frac{K_{IIIC}^2}{\mu} \end{Bmatrix}$$

1.3.2 Limitations of Linear Elastic Fracture Mechanics and its evolutions

The previous treatment implies stresses tending to the infinite close to the crack apex in contrast with the finite sigmap ultimate traction strength of the material. Figure 1.7 indicates the limitation of the stress state in the hypothesis of material with no hardening (that is, perfectly plastic, see Figure 1.7a)) and material with negative hardening (that is, softening type, see Figure 1.7b)).

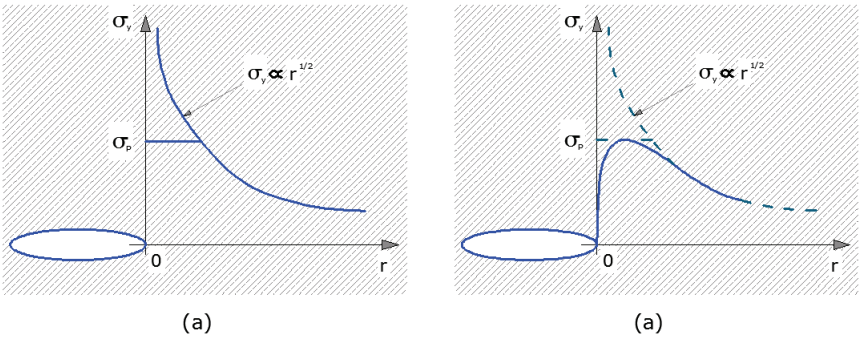

Figure 1.7. Limitation of the stress state close to the crack tip.

This behaviour implies the formation of a plastic zone in ductile materials, such as metals, and of a micro-cracked zone (known as the process zone) in brittle materials, such as concrete, rocks and ceramics. Linear Elastic Fracture Mechanics can only be applied when the plastic zone, or the micro-cracked zone, is small in comparison to the dimensions of the structure. This occurs in metals but does not generally occur in brittle materials. Various estimates of the length of the plastic zone have been proposed. The two best known are those of Irwin [16] and of Dugdale [20]. Irwin' s hypothesis is based on the redistribution of the elastic and plastic stresses close to the crack apex, which is obtained by transferring the distribution of the individual stresses (Figure 1.8).

This, from the graphic point of view, implies equality of the two areas highlighted in Figure 1.8 . The magnitude of the plastic zone is:

$$a_{PC} = \frac{K_{IC}^2}{\pi\ \sigma_P^2}$$

Dugdale's model is instead based on a constant distribution of the σ_P stresses on a fictitious crack of length a_P(Figure 1.9):

By applying the condition of vanishy of the stress intensity factor of the total strains (obtained as the sum of the stain due to the stress acting to infinity and that due to the constant distribution of stresses equal to σ_P) one obtains:

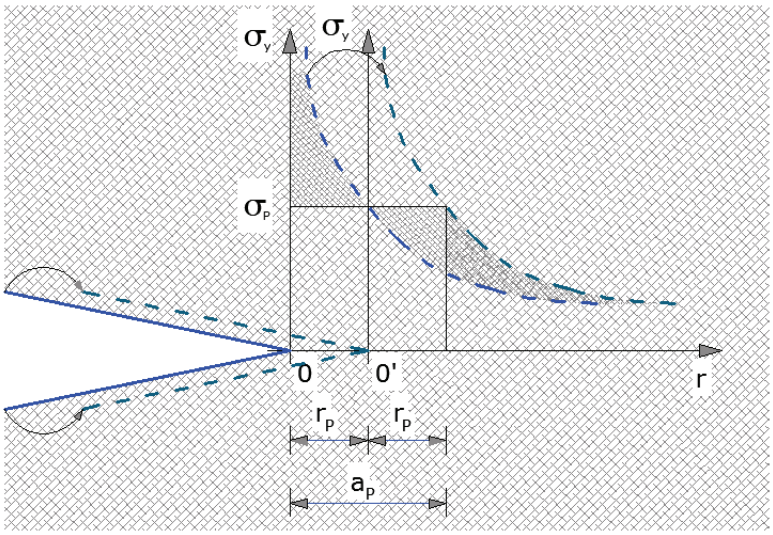

Figure 1.8. Irwin's hypothesis (redistribution of the plastic stresses).

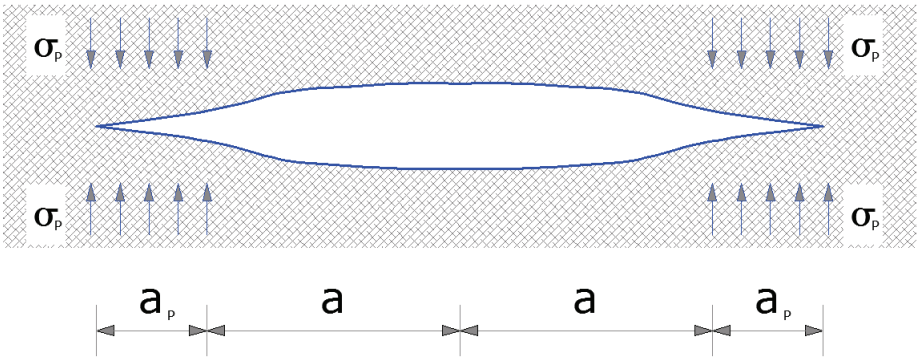

Figure 1.9. Dugdale's hypothesis (constant distribution of the stresses).

$$a_{PC} = \frac{\pi K_{IC}^2}{8\sigma_P^2}$$

The two estimates of a_p are different from each other for about 20%; a ductility ratio of the material of K_{IC}/σ_P is present in both.

An evolution of the previous models, proposed by Barenblatt [19] , [21] and Rice [17], is the Fictitious Crack Model, which will be dealt with in

the next chapter.

1.3.3 Scale effects and brittleness number

The physical dimensions of K_{IC} lead to the absence of physical similarity in the traction collapse of cracked solids that have constant geometrical ratios. One parameter that allows the ductility or fragility of a structure to be measured is the energy fragility number s_E , which depends on the fracture energy $\mathcal{G}_F$, on the ultimate traction strength σ_u and on a characteristic dimension of the structure itself [18], [22]:

$$s_E = \frac{\mathcal{G}_F}{\sigma_u \quad b}$$

Another dimensionless parameter, called the static fragility number s, can be written in function of toughness K_{IC}:

$$s = \frac{K_{IC}}{\sigma_u b^{1/2}}$$

The two fragility numbers are related through the relation:

$$s_E = s^2 \varepsilon_u$$

A similar parameter was introduced by Hillerborg, Modeer and Petersson [24] in the form of the characteristic length of elements in concrete:

$$l_0 = \frac{\mathcal{G}_F E}{f_t^2}$$

in which f_t represents the ultimate traction strength of the concrete. Similarity in the collapse is only possible for structures which have the same value as the fragility number.

1.4 Cohesive crack model

The Cohesive Model makes it possible to describe the behavior of materials with strain-softening behavior. Mode I problems are characterized by the

a priori knowledge of the trajectory of the crack, while in mixed Mode problems, this constitutes another unknown factor. In both cases, the finite element Method is an elegant way of facing crack propagation problems in materials; it takes into account effects such as the scale effect and the transition from ductile to brittle behaviour.

1.4.1 Fundamentals of the Cohesive Model

This model was proposed by Barenblatt [19] and Dugdale [20]. It was then studied by Bilby, Cottrell and Swinden [26], Willis [27] and Rice [17]. It has recently been re-proposed by Wnuk [28] under the name of Final Stretch Model, and by Hillerborg, Modeer and Petersson [25] under the name of Fictitious Crack Model. In 1985, Carpinteri re-proposed the primary denomination of Cohesive Crack Model [29],[30].

The basic hypothesis is that a fictitious crack forms, as a prolongation of the real crack, which is known as the process zone, in which the material, although damaged, is still able to transfer stresses (Figure 1.10).

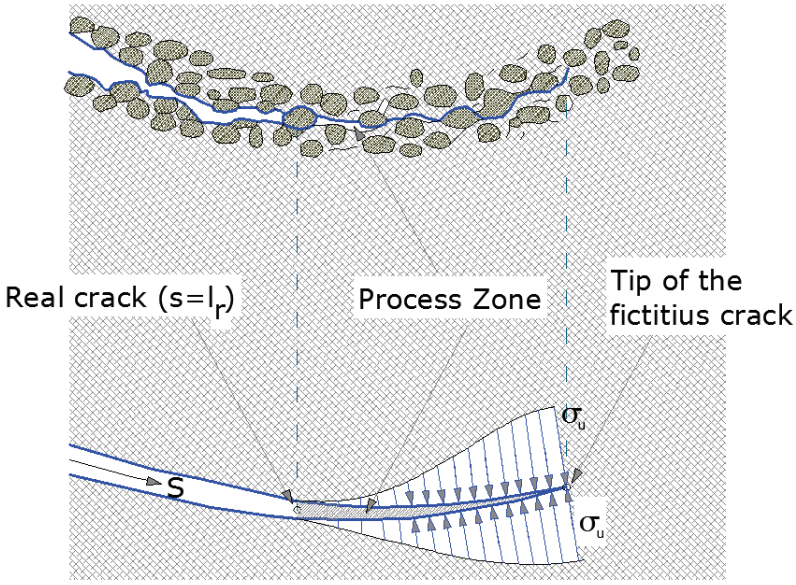

Figure 1.10. Process zone with reclosing stresses.

The point that separates the zone that is free of stresses, which is known as the real crack, from the process zone is called real crack tip, while the point that separates the process zone from the integral material is called fictitious crack tip. The process zone is the zone in which the energy dissipation occurs; it begins to develop when the main traction stress reaches the ultimate strength of the material σ_u in a perpendicular direction to the direction of the main traction stress.

Moreover, the material transmits stresses in the process zone that are linear and decreasing functions of the displacement discontinuity, while the material in the undamaged zone behaves in a linear elastic mode, as shown in Figure 1.11:

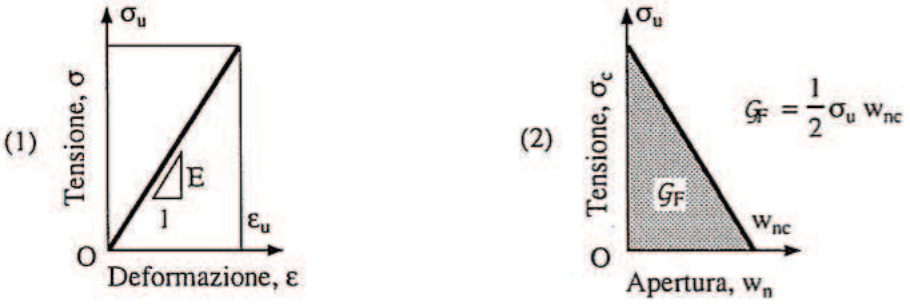

Figure 1.11. Constitutive laws (1): integral material, (2): process zone.

The area under the $\sigma - w_n$ curve represents the fracture energy $\mathcal{G}_f$. The stress is always equal to the value of the ultimate traction strength at the edge of the fictitious crack. Therefore, no singularities emerge in the stress state. The tangential stresses in the process zone were not considered in the described model. Fracture energy $\mathcal{G}_f$ and the ultimate traction strength σ_u are considered to be properties of the material: reference can be made to [31],[32] for more detailed analyses.

1.4.2 The Cohesive Model for Mode I problems

In this case, the trajectory of the crack is known, because of symmetry reasons. Proceeding in the spirit of the Finite Element Method, it is possible to build a grid with n couples of nodes arranged along the crack propagation direction [23], [33],[34]. The cohesive forces are therefore substituted by the nodal force F_i, whose intensity depends on the opening of the crack on the basis of the $\sigma - w_n$ constitutive law of the material.

Figure 1.12 shows the geometrical characteristics of a sample for a bending test at three points:

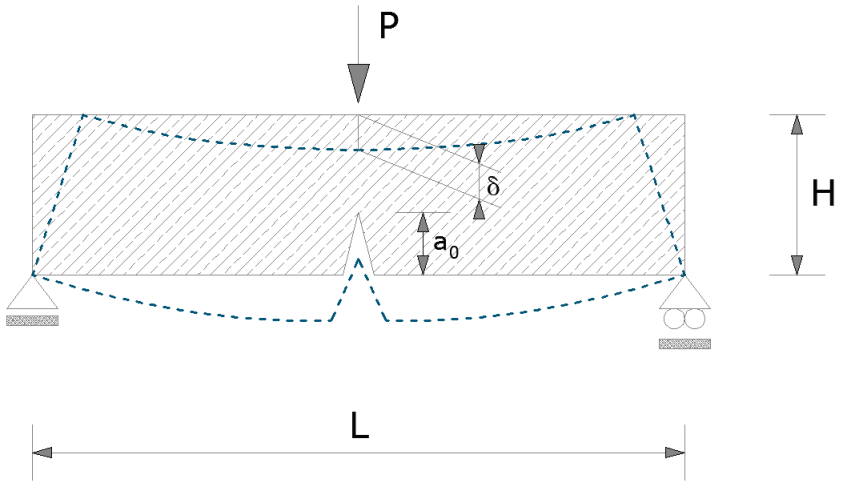

Figure 1.12. Three points Bending test.

Figure 1.13 shows the choice of the nodes (extended to about 9/100 the height of the sample) in the case of a bending test at three points.

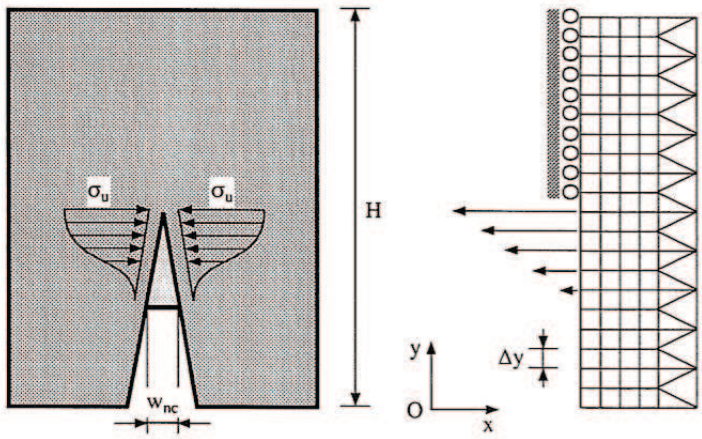

Figure 1.13. Schematization for the case of Three points Bending test.

The problem can be formulated as follows:

$$\mathbf{w} = \mathbf{H}\ \mathbf{F} + \mathbf{C}\ \mathbf{P} \tag{1.8}$$

in which **w** indicates the vector, of dimension n, that contains the crack opening, **H** is the matrix, of dimension n x n of the coefficients of influence corresponding to $F_i = 1$ and **C** is the vector of the coefficients of influence relative to an external unitary load P. The cohesive forces have an intensity value equal to:

- real crack ($w > w_{nc}$):

$$F_i = 0 \quad per \quad i = 1,2....,j-1 \tag{1.9}$$

- fictitious crack ($0 < w < w_{nc}$):

$$F_i = F_u\Big(1 - \frac{w_i}{w_{nc}}\Big) \quad per \quad i = j,....,m-1 \tag{1.10}$$

- tip of the fictitious crack ($w = 0$):

$$F_i = F_u \tag{1.11}$$

- intact material :

$$w_i = 0 \quad per \quad i = m+1,....,n \tag{1.12}$$

in which $t = the\ sample\ thickness$ and $\Delta_y =$ the distance between the couples of nodes. Altogether, the equations are $2n+1$ (n le 1.8 and $n+1$ le 1.9 - 1.12) in the $2n+1$ unknowns **w**,**F** . The lowering of the loading point is calculated with 1.13:

$$\delta = \mathbf{C^T}\ \mathbf{F}\ + D_P\ P \tag{1.13}$$

in which D_P represents the lowering of the loading point for $P = 1$. The equations of the system depend on the indices i (tip of the real crack) and m (tip of the fictitious crack), which vary according to the crack propagation process, and they are determined as follows:

1. At the first step, the process zone is absent and the tip of the real crack coincides with the tip of the incision for which $j = m$. If there is no incision, it coincides with $m = j = 1$.

2. At each step, the fictitious crack increases by the quantity Δ_y-, therefore m is increased by 1.

3. The $2n + 1$ equation system is resolved and the opening W_j is controlled from the tip of the real crack:

   - if $w_i \leq w_{nc}$: move to point (4),
   - if $w_j > w_{nc}$: increase j and control the remaining number of cohesive connections (equal to $m - j$):
     - $(m - j) \geq 4$: the problem is well-posed, return to point (3),
     - $(m - j) < 4$: the problem is too brittle. It is necessary to thicken the grid (by increasing n) and to repeat the analysis.

4. Check that $F < F_u$ in the intact material and $w < w_{nc}$ in the process zone.

5. Calculate the lowering δ of the loading point on the basis of (1.13).

6. If $m < n$, return to point (2), otherwise the analysis comes to an end.

In elastic and elasto-plastic models, the zones in which the stress and strain functions are continuous and derivable coincide: this does not occur in the Cohesive Model in that the stresses are continuous and the strains discontinuous in the process zone. Moreover, the stress state is known during the crack growing process, at the apex of the fictitious crack. The main traction stress at this point is in fact equal to the value of the ultimate traction strength of the material σ_u. The model makes it possible to describe the phenomena of the scale effect and of the ductile-brittle transition, as shown in the following chapter. The collapse caused by the propagation of the crack, described by Linear Elastic Fracture Mechanics, is interpreted

by the Cohesive Model as a catastrophic type of collapse, characterized by a softening branch which has a positive slope, and which is known as snap-back. An analytical way of determining the maximum load and the critical dimensions (so as not to determine snap-back) of the Cohesive Model in Mode 1 problems is presented in [35],[36].

Chapter 2

Asymptotic field at the tip of the bi-material interface

2.1 Introduction

Cohesive crack models are an important means of describing localisation and failure in engineering structures,with reference to quasi-brittle materials. When these models are adopted, the stresses acting on the non-linear fracture process zone are considered as decreasing functions of the displacement discontinuity. These functions are assumed to be material properties through the use of a pre-defined softening law. Although this standard formulation of the cohesive crack model is higly semplified, it is able to capture the essence of the fracture process in concrete specimens and structures (see [48]). De Borst [49] have given an overview of the various ways of numerically implement the cohesive zone method. They concluded that the extended/generalized finite element method (XFEM) ([50] , [51] , [52]) provides a proper representation of the discrete character of the method avoiding any mesh bias. The XFEM enriches the standard local FE approximations with known information about the problem. Zi and Belytschko [53] enriched all cracked linear or quadratic triangular elements including the elements containing the crack tip by the sign function.

Alfaiate et al. [54] embedded displacements jumps which do not need to be homogeneous within each FE. Mariani and Perego [55] introduced in a standard FE model a displacement discontinuity, in order to riproduce the typical cusp-like shape of the process zone at the tip of a cohesive crack. However the cubic function does not represent the true angular distribution of the displacement adjacent to the tip. In order to overcome this problem Karihaloo and Xiao [56] obtained an asymptotic expansion at the cohesive crack tip, analogous to Williams expansions at a traction free crack tip. Coulomb friction on the cohesive crack faces is also considered. The main advantage of the above mentioned expansion compared to the work of Zhang and Deng [57], is that the softening law can be expressed in a special polinomial form which can be calibrated on many commonly-used traction-separation law, e.g. rectangular, linear, bilinear and exponential. Many studies on mixed mode cohesive cracks can be found in the litterature, for example , Valente [58] and Cocchetti et al [59], but there is doubt about the accuracy of the cohesion-sliding relation because it is difficult to isolate it from frictional forces between the rough cohesive crack faces in quasi-brittle materials such as concrete. The frictional cohesive cracks are different from the frictional contact of crack faces because the friction operates when the crack faces are open. A new asymptotic expansion, which can be applied at a bi-material interface,is presented in this paper with reference to the joint between a gravity dam and the foundation rock (see [60], [61], [62],[63] and [64]).

2.2 The Model

Theoretical investigations on the problem of interface cracks between dissimilar media date back to the late fifties. Williams [65] performed an asymptotic analysis of the elastic fields at the tip of an open interface crack and found that the stresses and displacements behave in a oscillatory manner.Malyshev and Salganik [66] discussed the implications of the oscillatory fields and made the following comment:"For opposite faces of the cut, the

result is physically absurd that is they are penetrating each other.The fault of the mathematical model can be corrected if it is supposed that the opposite faces taking mutually convex shapes start to press into each other forming contacting areas". They also argued that, if the length of the cohesive zone in a Barenblatt-Dugdale type model is greater than the region of stress oscillations,the latter can be disregarded near the crack tip.

2.2.1 Polynomial cohesive law for quasi-brittle materials

In order to obtain a separable asymptotic field at a cohesive crack tip, in terms of r and θ functions, (see Figure 2.1) in quasi-brittle materials, the softening law has been reformulated into the following polynomial form:

$$\frac{\sigma_y}{\sigma_0} = \frac{\tau_{xy}}{\mu_f \sigma_0} = 1 + \sum_{i=1}^{L} \alpha_i \left(\frac{w_{eff}}{w_{eff,c}} \right)^{\frac{(2i-1)}{3}} - \left(1 + \sum_{i=1}^{L} \alpha_i \right) \left(\frac{w_{eff}}{w_{eff,c}} \right)^{\frac{2L+1}{3}} \quad (2.1)$$

where $(\sigma_0, -\mu_f \sigma_0)$ is a point on the failure envelope, α_i,$i = 1...L$,are fitting parameters and σ_y is the stress normal to the cohesive crack faces;w_{eff} and $w_{eff,c}$ are the effective opening displacement of the cohesive crack faces and its critical value,respectively.

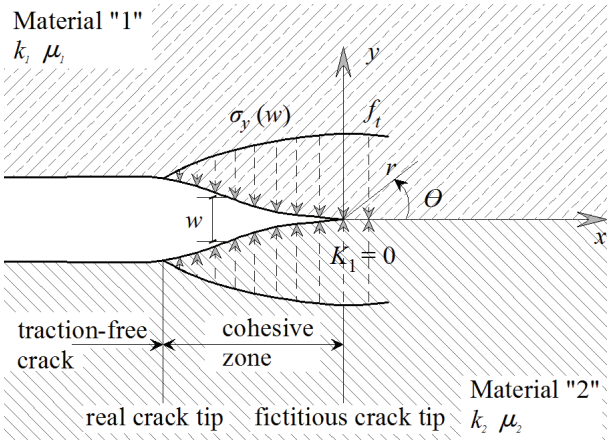

Figure 2.1. A traction free crack at a bi-material interface

Eq. (2.1) can represent a wide variety of softening laws,e.g. rectangular, linear, bilinear and exponential. Eq. (2.1) satisfies the following requirements:for $w_{eff}/w_{eff,c} = 0$ one obtains $\sigma_y/\sigma_0 = 1$ at the tip of the cohesive crack (fictitious crack tip,shortening FCT) ; and for $w_{eff}/w_{eff,c} = 1$ one obtains $\sigma_y/\sigma_0 = 0$ (see Figure 2.1) at the tip of the pre-existing traction-free macrocrack(real crack tip). In the present paper,the softening law proposed in [56] has been used with the coefficients:$\alpha_1 = -0.138471$,$\alpha_2 = -7.837117$,$\alpha_3 = 20.918546$,$\alpha_4 = -25.079296$ and $\alpha_5 = 14.148416$ see Figure 2.2 and Appendix A.An interesting experimental setup, which is able to check the path-dependent behaviour of the fracture process zone loaded in tensile and shear conditions is presented by Hassanzadeh [67].

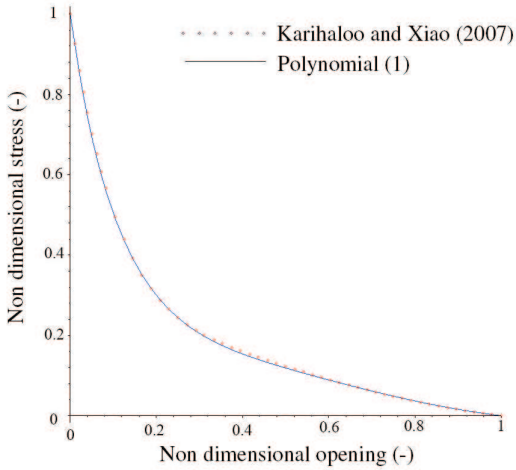

Figure 2.2. Cohesive law comparison

2.2.2 Asymptotic fields at the tip of a cohesive crack

The adopted mathematical formulation closely follows that used by Karihaloo and Xiao [56]. Muskhelishvili showed that, for plane problems, the stress and displacements in the Cartesian coordinate system can be expressed in terms of two analytic functions, $\phi(z)$ and $\chi(z)$, of the complex variable $z = re^{i\theta}$

$$\sigma_x + \sigma_y = 2[\phi'(z) + \overline{\phi'(z)}] \tag{2.2}$$

$$\sigma_y - \sigma_x + 2i\tau_{xy} = 2[\overline{z}\phi''(z) + \chi''(z)] \tag{2.3}$$

$$2\mu(u + iv) = k\phi(z) - z\overline{\phi'(z)} - \overline{\chi'(z)} \tag{2.4}$$

where a prime denotes differentiation with respect to z and an overbar denotes a complex coniugate. In Eq. (2.4), $\mu = E/[2(1+\nu)]$ is the shear modulus; the Kolosov constant is $\kappa = 3 - 4\nu$ for plane strain and $\kappa = (3-\nu)/(1+\nu)$ for plane stress; E and ν are Young's modulus and Poisson's ratio, respectively. For a general mixed mode I+II problem, the two analytic functions $\phi(z)$ and $\chi(z)$ can be chosen as series of complex eigenvalue Goursat functions (Sih and Liebowitz [68])

$$\phi_1(z) = \sum_{n=0} A_n z^{\lambda_n} = \sum_{n=0} A_n r^{\lambda_n} e^{i\lambda_n\theta}, \tag{2.5}$$

$$\chi_1(z) = \sum_{n=0} B_n z^{\lambda_n+1} = \sum_{n=0} B_n r^{\lambda_n+1} e^{i(\lambda_n+1)\theta} \tag{2.6}$$

$$\phi_2(z) = \sum_{n=0} G_n z^{\lambda_n} = \sum_{n=0} G_n r^{\lambda_n} e^{i\lambda_n\theta}, \tag{2.7}$$

$$\chi_2(z) = \sum_{n=0} H_n z^{\lambda_n+1} = \sum_{n=0} H_n r^{\lambda_n+1} e^{i(\lambda_n+1)\theta} \tag{2.8}$$

Eqs. (2.5) and (2.6) is applied to material 1 (see Figure 2.1 when ($0 \leq \theta \leq \pi$)):

$$\begin{aligned} 2\mu_1 u = \sum_{n=0} r^{\lambda_n} \{ & k_1(a_{1n}\cos\lambda_n\theta - a_{2n}\sin\lambda_n\theta) \\ & + \lambda_n[-a_{1n}\cos(\lambda_n - 2)\theta + a_{2n}\sin(\lambda_n - 2)\theta] \\ & + (\lambda_n + 1)(-b_{1n}\cos\lambda_n\theta + b_{2n}\sin\lambda_n\theta)\} \end{aligned} \tag{2.9}$$

$$2\mu_1 v = \sum_{n=0} r^{\lambda_n} \{k_1(a_{1n}\sin\lambda_n\theta + a_{2n}\cos\lambda_n\theta)$$

$$+\lambda_n[a_{1n}\sin(\lambda_n-2)\theta+a_{2n}\cos(\lambda_n-2)\theta] \tag{2.10}$$
$$+(\lambda_n+1)(b_{1n}\sin\lambda_n\theta+b_{2n}\cos\lambda_n\theta)\}$$

$$\sigma_x=\sum_{n=0} r^{\lambda_n-1}\{2\lambda_n[a_{1n}\cos(\lambda_n-1)\theta-a_{2n}\sin(\lambda_n-1)\theta]$$
$$-\lambda_n(\lambda_n-1)[a_{1n}\cos(\lambda_n-3)\theta-a_{2n}\sin(\lambda_n-3)\theta] \tag{2.11}$$
$$-(\lambda_n+1)\lambda_n[b_{1n}\cos(\lambda_n-1)\theta-b_{2n}\sin(\lambda_n-1)\theta]\}$$

$$\sigma_y=\sum_{n=0} r^{\lambda_n-1}\{2\lambda_n[a_{1n}\cos(\lambda_n-1)\theta-a_{2n}\sin(\lambda_n-1)\theta]$$
$$+\lambda_n(\lambda_n-1)[a_{1n}\cos(\lambda_n-3)\theta-a_{2n}\sin(\lambda_n-3)\theta] \tag{2.12}$$
$$+(\lambda_n+1)\lambda_n[b_{1n}\cos(\lambda_n-1)\theta-b_{2n}\sin(\lambda_n-1)\theta]\}$$

$$\tau_{xy}=\sum_{n=0} r^{\lambda_n-1}\{\lambda_n(\lambda_n-1)[a_{1n}\sin(\lambda_n-3)\theta+a_{2n}\cos(\lambda_n-3)\theta] \tag{2.13}$$
$$+(\lambda_n+1)\lambda_n[b_{1n}\sin(\lambda_n-1)\theta+b_{2n}\cos(\lambda_n-1)\theta]\}$$

while Eqs. (2.7) and (2.8) is applied to material 2 (-$\pi \le \theta \le 0$).

$$2\mu_2 u=\sum_{n=0} r^{\lambda_n}\{k_2(g_{1n}\cos\lambda_n\theta-g_{2n}\sin\lambda_n\theta)$$
$$+\lambda_n[-g_{1n}\cos(\lambda_n-2)\theta+g_{2n}\sin(\lambda_n-2)\theta] \tag{2.14}$$
$$+(\lambda_n+1)(-h_{1n}\cos\lambda_n\theta+h_{2n}\sin\lambda_n\theta)\}$$

$$2\mu_2 v=\sum_{n=0} r^{\lambda_n}\{k_2(g_{1n}\sin\lambda_n\theta+g_{2n}\cos\lambda_n\theta)$$
$$+\lambda_n[g_{1n}\sin(\lambda_n-2)\theta+g_{2n}\cos(\lambda_n-2)\theta] \tag{2.15}$$
$$+(\lambda_n+1)(h_{1n}\sin\lambda_n\theta+h_{2n}\cos\lambda_n\theta)\}$$

$$\begin{aligned}\sigma_x = \sum_{n=0} r^{\lambda_n-1}\{&2\lambda_n[g_{1n}\cos(\lambda_n-1)\theta - g_{2n}\sin(\lambda_n-1)\theta]\\ &-\lambda_n(\lambda_n-1)[g_{1n}\cos(\lambda_n-3)\theta - g_{2n}\sin(\lambda_n-3)\theta]\\ &-(\lambda_n+1)\lambda_n[h_{1n}\cos(\lambda_n-1)\theta - h_{2n}\sin(\lambda_n-1)\theta]\}\end{aligned} \tag{2.16}$$

$$\begin{aligned}\sigma_y = \sum_{n=0} r^{\lambda_n-1}\{&2\lambda_n[g_{1n}\cos(\lambda_n-1)\theta - g_{2n}\sin(\lambda_n-1)\theta]\\ &+\lambda_n(\lambda_n-1)[g_{1n}\cos(\lambda_n-3)\theta - g_{2n}\sin(\lambda_n-3)\theta]\\ &+(\lambda_n+1)\lambda_n[h_{1n}\cos(\lambda_n-1)\theta - h_{2n}\sin(\lambda_n-1)\theta]\}\end{aligned} \tag{2.17}$$

$$\begin{aligned}\tau_{xy} = \sum_{n=0} r^{\lambda_n-1}\{&\lambda_n(\lambda_n-1)[g_{1n}\sin(\lambda_n-3)\theta + g_{2n}\cos(\lambda_n-3)\theta]\\ &+(\lambda_n+1)\lambda_n[h_{1n}\sin(\lambda_n-1)\theta + h_{2n}\cos(\lambda_n-1)\theta]\}\end{aligned} \tag{2.18}$$

The complex coefficients are $A_n = a_{1n} + ia_{2n}$,$B_n = b_{1n} + ib_{2n}$,$G_n = g_{1n} + ig_{2n}$ and $H_n = h_{1n} + ih_{2n}$. The eingenvalues, λ_n and coefficients a_{1n},a_{2n},b_{1n},b_{2n},g_{1n},g_{2n},h_{1n} and h_{2n} are real. By substituting the complex functions (2.5) in Eqs. (2.2), (2.3) and (2.4) , the complete series expansion of the displacements and stresses near the tip of the crack can be written exactly as in Karihaloo and Xiao [56].The coefficients a_{1n},a_{2n},b_{1n} and b_{2n} are used in the case of material 1. The coefficients g_{1n},g_{2n},h_{1n} and h_{2n} are used for material 2 [69].

2.2.3 The conditions at the bi-material interface

The opening displacement (COD) of the crack faces can be written as $w = v\Big|_{\theta=\pi} - v\Big|_{\theta=-\pi}$:

$$\begin{aligned}w = \sum_{n=0} \frac{r^{\lambda_n}}{2}\Bigg[&\frac{k_1+\lambda_n}{\mu_1}a_{1n} + \frac{\lambda_n+1}{\mu_1}b_{1n} +\\ &+\frac{k_2+\lambda_n}{\mu_2}g_{1n} + \frac{\lambda_n+1}{\mu_2}h_{1n}\Bigg]\sin\lambda_n\pi\end{aligned} \tag{2.19}$$

and the sliding displacement (CSD) can be written as $\delta = u\Big|_{\theta=\pi} - u\Big|_{\theta=-\pi}$:

$$\delta = \sum_{n=0} \frac{r^{\lambda_n}}{2} \left[\frac{\lambda_n - k_1}{\mu_1} a_{2n} + \frac{\lambda_n + 1}{\mu_1} b_{2n} + \right. \\ \left. + \frac{\lambda_n - k_2}{\mu_2} g_{2n} + \frac{\lambda_n + 1}{\mu_2} h_{2n} \right] \sin \lambda_n \pi \quad (2.20)$$

The formulation of the problem shown in Figure 4.3 can be assessed by establishing continuity, in terms of stress and displacement, when $\theta = 0$ (the two materials are bonded along the line of the crack extension), and when $\theta = \pm\pi$ (cohesive crack surfaces). The stresses at the cohesive crack tip are non-singular (because the stress intensity factors are $K_1 = K_2 = 0$). The above mentioned conditions can be summarised as follows.

2.2.4 Cohesive frictional crack with normal cohesive separation

The following conditions need to be satisfied ($\theta = \pm 0$, two materials are bonded):

$$u|_{\vartheta=0^+} = u|_{\vartheta=0^-} \quad (2.21)$$

$$v|_{\vartheta=0^+} = v|_{\vartheta=0^-} \quad (2.22)$$

$$\sigma_y|_{\vartheta=0^+} = \sigma_y|_{\vartheta=0^-} \quad (2.23)$$

$$\tau_{xy}|_{\vartheta=0^+} = \tau_{xy}|_{\vartheta=0^-} \quad (2.24)$$

Eq. (2.21) to Eq. (2.24) give:

$$\frac{1}{\mu_1}[(k_1 - \lambda_n)a_{1n} - (\lambda_n + 1)b_{1n}] = \frac{1}{\mu_2}[(k_2 - \lambda_n)g_{1n} - (\lambda_n + 1)h_{1n}] \quad (2.25)$$

$$\frac{1}{\mu_1}[(k_1 + \lambda_n)a_{2n} + (\lambda_n + 1)b_{2n}] = \frac{1}{\mu_2}[(k_2 + \lambda_n)g_{2n} + (\lambda_n + 1)h_{2n}] \quad (2.26)$$

$$a_{1n} + b_{1n} = g_{1n} + h_{1n} \tag{2.27}$$

$$(\lambda_n - 1)a_{2n} + (\lambda_n + 1)b_{2n} = (\lambda_n - 1)g_{2n} + (\lambda_n + 1)h_{2n} \tag{2.28}$$

The continuity of u guarantees that of ε_x. For each value of λ_n, the asymptotic fields in material 1 are characterized by a vector of 4 unknowns $[a_{1n},a_{2n},b_{1n},b_{2n}]$; similarly, in material 2 they are characterized by a second vector $[g_{1n},g_{2n},h_{1n},h_{2n}]$.The Eqs. (2.25) to (2.28) give the following constraints on the coefficients:

$$g_{1n}= \left(\frac{\mu_2(k_1 - \lambda_n)}{(k_2 + 1)\mu_1} + \frac{\lambda_n + 1}{k_2 + 1}\right) a_{1n} + \left(\frac{\mu_2(-\lambda_n - 1)}{(k_2 + 1)\mu_1} + \frac{\lambda_n + 1}{k_2 + 1}\right) b_{1n} \tag{2.29}$$

$$g_{2n}= \left(\frac{\mu_2(k_1 + \lambda_n)}{(k_2 + 1)\mu_1} + \frac{1 - \lambda_n}{k_2 + 1}\right) a_{2n} + \left(\frac{\mu_2(\lambda_n + 1)}{(k_2 + 1)\mu_1} - \frac{\lambda_n + 1}{k_2 + 1}\right) b_{2n} \tag{2.30}$$

$$h_{1n} = \left(\frac{-\mu_2(k_1 - \lambda_n)}{(k_2 + 1)\mu_1} + \frac{k_2 - \lambda_n}{k_2 + 1}\right) a_{1n} + \\ + \left(\frac{\mu_2(\lambda_n + 1)}{(k_2 + 1)\mu_1} + \frac{k_2 - \lambda_n}{k_2 + 1}\right) b_{1n} \tag{2.31}$$

$$h_{2n} = \left(\frac{(1 - \lambda_n)\mu_2(k_1 + \lambda_n)}{(k_2 + 1)(\lambda_n + 1)\mu_1} + \frac{(k_2 + \lambda_n)(\lambda_n - 1)}{(k_2 + 1)(\lambda_n + 1)}\right) a_{2n} + \\ + \left(\frac{(1 - \lambda_n)\mu_2}{(k_2 + 1)\mu_1} + \frac{(k_2 + \lambda_n)}{(k_2 + 1)}\right) b_{2n} \tag{2.32}$$

The following conditions need to be satisfied along the cohesive zone ($\theta = \pm\pi$):

$$\sigma_y|_{\vartheta=\pi} = \sigma_y|_{\vartheta=-\pi} \neq 0 \tag{2.33}$$

$$\tau_{xy}|_{\theta=\pi} = \tau_{xy}|_{\theta=-\pi} = -\mu_f \sigma_y|_{\vartheta=\pi} \neq 0 \tag{2.34}$$

where μ_f equals the positive or negative value of the of kinetic friction coefficient, which is assumed to be constant, and to depend on the relative

sliding direction of the two crack edges. In other words, $\mu_f > 0$ when $\delta < 0$ and $\mu_f < 0$ when $\delta > 0$.

Eqs. (2.33) and (2.34) give:

$$(a_{2n} + b_{2n} + g_{2n} + h_{2n}) \sin((\lambda_n - 1)\pi) = 0 \tag{2.35}$$

$$[(\lambda_n - 1)(a_{1n} + g_{1n}) + (\lambda_n + 1)(b_{1n} + h_{1n})] \sin((\lambda_n - 1)\pi) = 0 \tag{2.36}$$

$$\begin{aligned}\{[g_{2n}+h_{2n}+\mu_f(a_{1n}+b_{1n})]\lambda_n+[-g_{2n}+h_{2n}+\mu_f(a_{1n}+b_{1n})]\} \cos((\lambda_n-1)\pi)+ \\ + \{[g_{1n} + h_{1n} + \mu_f(a_{2n} + b_{2n})]\lambda_n + [-g_{1n} + h_{1n}+ \\ + \mu_f(a_{2n} + b_{2n})]\} \sin((\lambda_n - 1)\pi) = 0\end{aligned} \tag{2.37}$$

Eqs. (2.35) , (2.36) and (2.37) show that the asymptotic solution is composed of two parts:

(a) if $\sin((\lambda_n - 1)\pi) = 0$, Eq. (2.37) requires:

$$\{[g_{2n} + h_{2n} + \mu_f(a_{1n} + b_{1n})]\lambda_n + [-g_{2n} + h_{2n} + \mu_f(a_{1n} + b_{1n})]\} = 0 \tag{2.38}$$

This part of the solution is characterized by integer eigenvalues.

(b) if $\cos((\lambda_n - 1)\pi) = 0$, Eqs. (2.35) , (2.36) and (2.37) require:

$$(a_{2n} + b_{2n} + g_{2n} + h_{2n}) = 0 \tag{2.39}$$

$$[(\lambda_n - 1)(a_{1n} + g_{1n}) + (\lambda_n + 1)(b_{1n} + h_{1n})] = 0 \tag{2.40}$$

$$[g_{1n} + h_{1n} + \mu_f(a_{2n} + b_{2n})]\lambda_n + [-g_{1n} + h_{1n} + \mu_f(a_{2n} + b_{2n})] = 0 \tag{2.41}$$

This part of the solution is characterized by fractional eigenvalues.

(a) *Integer eigenvalues*

$$\lambda_n = n + 1, \qquad n = 0,1,2,... \tag{2.42}$$

Equation (2.38) give:

$$na_{2n} + (n + 2)b_{2n} = -\mu_f(n + 2)(a_{1n} + b_{1n}, \qquad n = 0,1,2,... \tag{2.43}$$

From Eq. (2.43), we have:

$$b_{2n} = -\frac{n}{n+2} a_{2n} - \mu_f (a_{1n} + b_{1n})$$

giving

$$\sigma_y|_{\vartheta=\pm\pi} = \sum_{n=0} r^n (n+2)(n+1)(a_{1n} + b_{1n})\ cos(n\pi) \tag{2.44}$$

or

$$\hat{\sigma_y} = \frac{\sigma_y|_{\vartheta=\pm\pi}}{\sigma_0} = \sum_{n=0} c_n r^n = 1 + \sum_{n=1} c_n r^n \tag{2.45}$$

where

$$c_n = \frac{(n+2)(n+1)(a_{1n} + b_{1n})\ cos(n\pi)}{\sigma_0} \tag{2.46}$$

Since g_{1n} and h_{1n} can be written as functions of a_{1n} and b_{1n} cite through Eq. (2.25) and (2.27) ,the same expression used in the homogeneous case can hold ($w = \delta = 0$).

For $\lambda_0 = 1$, one obtains $\sigma_0 = a_{10} + b_{10}$, $\mu_f \sigma_0 = 2b_{20}$ and $\sigma_x|_{\vartheta=0} = 2a_{10} - 2b_{10}$.

(b) *Fractional eigenvalues*

$$\lambda_n = n + \frac{3}{2}, \qquad n = 0,1,2,... \tag{2.47}$$

Eqs. (2.26) and (2.28) allow one to express g_{2n} and h_{2n} as functions of a_{2n} and b_{2n} [69].

Therefore, Eq. (2.35) gives:

$$b_{2n} = -\frac{(\mu_1 k_2 \lambda_n + \mu_1 + \mu_2 k_1 + \mu_2 \lambda_n)}{(\mu_2 \lambda_n + \mu_2 + \mu_1 k_2 \lambda_n + \mu_1 k_2)} a_{2n} \tag{2.48}$$

Eqs. (2.25) and (2.27) allow one to express g_{1n} and h_{1n} as functions of a_{1n} and b_{1n} [69].

Therefore, Eq. (2.36)gives:

$$b_{1n} = \frac{(-\mu_1 k_2 \lambda_n + \mu_1 + \mu_2 k_1 - \mu_2 \lambda_n)}{(\mu_2 \lambda_n + \mu_2 + \mu_1 k_2 \lambda_n + \mu_1 k_2)} a_{1n} \tag{2.49}$$

and Eqs. (2.48) and Eq. (2.49) in Eq. (2.41) give:

$$a_{2n} = -\frac{a_{1n}}{\mu_f} \tag{2.50}$$

Substituting Eqs (2.48), (2.49) and (2.50) in Eqs. (2.2) and (2.3) gives:

$$\sigma_y|_{\vartheta=\pm\pi} = \\ = \sum_{n=0} r^{\frac{2n+1}{2}} \left[\frac{2n+3}{2} \left(\frac{\mu_2(k_1-1) - \mu_1(k_2-1)}{\mu_2 + \mu_1 k_2} \right) a_{2n} \right] \sin \frac{2n+3}{2}\pi \tag{2.51}$$

$$\tau_{xy}|_{\vartheta=\pm\pi} = \\ = \sum_{n=0} r^{\frac{2n+1}{2}} \left[\frac{2n+3}{2} \left(\frac{\mu_2(k_1-1) - \mu_1(k_2-1)}{\mu_2 + \mu_1 k_2} \right) a_{1n} \right] \sin \frac{2n+3}{2}\pi \tag{2.52}$$

$$\hat{\sigma_y} = \frac{\sigma_y|_{\vartheta=\pm\pi}}{\sigma_0} = \frac{\tau_{xy}|_{\vartheta=\pm\pi}}{-\mu_f \sigma_0} = \sum_{n=0} e_n r^{\frac{2n+1}{2}} \tag{2.53}$$

where

$$e_n = \frac{1}{\sigma_0} \left[\frac{2n+3}{2} \left(\frac{\mu_2(k_1-1) - \mu_1(k_2-1)}{\mu_2 + \mu_1 k_2} \right) a_{2n} \right] \sin \frac{2n+3}{2}\pi \tag{2.54}$$

It is worthwhile noting that the e_n coefficients vanish in the homogeneous case.This is the main difference between the two cases.

Substituting Eqs (2.48), (2.49) and (2.50) in Eqs (2.19) and (2.20) gives

$$w = \sum_{n=0} r^{\frac{2n+3}{2}} \left[\frac{2(\mu_1 + \mu_2 k_1)}{\mu_1 \mu_2} a_{1n} \right] \sin \frac{2n+3}{2}\pi \tag{2.55}$$

$$\delta = \sum_{n=0} r^{\frac{2n+3}{2}} \left[-\frac{2(k_1k_2-1)}{\mu_1 k_2 - \mu_2} a_{2n} \right] \sin\frac{2n+3}{2}\pi \tag{2.56}$$

According to the well established literature on the mechanical behaviour of concrete joints (see Cervenka et al. [41]),softening only depends on $w_{eff} = \sqrt{w^2+\delta^2}$:

$$\sum_{n=0} r^{\frac{2n+3}{2}} 2\left(\frac{(\mu_1+\mu_2 k_1)^2}{(\mu_1\mu_2)^2} a_{1n}^2 + \frac{(k_1k_2-1)^2}{\mu_1^2 k_2^2 - \mu_2^2} a_{2n}^2 \right)^{1/2} \sin\frac{2n+3}{2}\pi \tag{2.57}$$

$$\hat{w} = \frac{w_{eff}}{w_{eff,c}} = \sum_{n=0} r^{\frac{2n+3}{2}} \bar{d}_n \tag{2.58}$$

$$\bar{d}_n = 2\left(\frac{(\mu_1+\mu_2 k_1)^2}{(\mu_1\mu_2)^2} a_{1n}^2 + \frac{(k_1k_2-1)^2}{\mu_1^2 k_2^2 - \mu_2^2} a_{2n}^2 \right)^{1/2} \sin\frac{2n+3}{2}\pi \tag{2.59}$$

Let us consider the truncated $N+1$ terms of $\hat{w}$ (2.59), and denote $d_0 = \bar{d}_0$,$d_n = \bar{d}_n/d_0$ $(n>1)$

$$\hat{w} = d_0 r^{\frac{3}{2}} \left(1 + \sum_{n=1}^{N} d_n r^n \right) \tag{2.60}$$

From this relation, we can obtain:

$$\hat{w}^{\frac{(2i-1)}{3}} = \left(\frac{w_{eff}}{w_c} \right)^{\frac{(2i-1)}{3}} = d_0^{\frac{(2i-1)}{3}} r^{\frac{(2i-1)}{2}} \left(1 + \sum_{n=1}^{N} d_n r^n \right)^{\frac{(2i-1)}{3}} \tag{2.61}$$

$$\hat{w}^{\frac{(2i-1)}{3}} = d_0^{\frac{(2i-1)}{3}} r^{\frac{(2i-1)}{2}} \left(1 + \sum_{n=1}^{M} \beta_{in} r^n \right), \qquad (M \geq N)) \tag{2.62}$$

in which:

$$\beta_{in} = \frac{f_i^{(n)}(0)}{n!}, \quad f_i(r) = \left(1 + \sum_{n=1}^{N} d_n r^n \right)^{\frac{(2i-1)}{3}} \tag{2.63}$$

where $f_i^{(n)}(0)$ denotes the nth derivative at $r = 0$. We now substitute Eq. (2.62) in the right hand side of Eq. (2.1), and Eq. (2.53) and a constant stress term in its left hand side.

In this way we obtain:

$$\hat{\sigma_y} = \left(\frac{\sigma_y}{\sigma_0}\right) = \left(\frac{\tau_{xy}}{\mu_f \sigma_0}\right) = 1 + \sum_{n=1} e_n r^{\frac{2n+1}{2}} = \\ = 1 + \sum_{i=1}^{L} \alpha_i {d_0}^{\frac{2i-1}{3}} r^{\frac{2i-1}{2}} \left(1 + \sum_{n=1}^{M} \beta_{in} r^n\right) - \\ + \left(1 + \sum_{i=1}^{L} \alpha_i\right) {d_0}^{\frac{2L+1}{3}} r^{\frac{2L+1}{2}} \left(1 + \sum_{n=1}^{M} \beta_{(\frac{2L+1}{2})n} r^n\right) \quad (2.64)$$

Through a term by term comparison applied to Eq. (2.64), we obtain the relations between the coefficients e_i , α_i and β_{in}.

(1) L=1

$$e_1 = \alpha_1 {d_0}^{1/3} \quad (2.65)$$
$$e_2 = \alpha_1 {d_0}^{1/3} \beta_{1,1} - (1 + \alpha_1) d_0 \quad (2.66)$$
$$e_3 = \alpha_1 {d_0}^{1/3} \beta_{1,2} - (1 + \alpha_1) d_0 \beta_{3/2,1} \quad (2.67)$$

(2) L=2

$$e_1 = \alpha_1 d_0^{1/3} \quad (2.68)$$
$$e_2 = \alpha_1 {d_0}^{1/3} \beta_{1,1} + \alpha_2 d_0 \quad (2.69)$$
$$e_3 = \alpha_1 {d_0}^{1/3} \beta_{1,2} + \alpha_2 d_0 \beta_{2,1} - (1 + \alpha_1 + \alpha_2) {d_0}^{5/3} \quad (2.70)$$
$$e_4 = \alpha_2 d_0 \beta_{2,2} - (1 + \alpha_1 + \alpha_2) {d_0}^{5/3} \beta_{5/2,1} \quad (2.71)$$

(3) L=3

$$e_1 = \alpha_1 d_0^{1/3} \tag{2.72}$$

$$e_2 = \alpha_1 {d_0}^{1/3} \beta_{1,1} + \alpha_2 d_0 \tag{2.73}$$

$$e_3 = \alpha_1 {d_0}^{1/3} \beta_{1,2} + \alpha_2 d_0 \beta_{2,1} + \alpha_3 {d_0}^{5/3} \tag{2.74}$$

$$e_4 = \alpha_1 {d_0}^{1/3} \beta_{1,3} + \alpha_2 d_0 \beta_{2,2} + \alpha_3 {d_0}^{5/3} \beta_{3,1} + \\ - \left(1 + \alpha_1 + \alpha_2 + \alpha_3\right) {d_0}^{7/3} \tag{2.75}$$

$$e_5 = \alpha_1 {d_0}^{1/3} \beta_{1,4} + \alpha_2 d_0 \beta_{2,3} + \alpha_3 {d_0}^{5/3} \beta_{3,2} + \\ - \left(1 + \alpha_1 + \alpha_2 + \alpha_3\right) {d_0}^{7/3} \beta_{7/2,1} \tag{2.76}$$

The previous coefficients e_i can be written by means of the following general expressions:

- when $L > n$

$$e_n = \sum_{i=1}^{n+1} \alpha_i d_0^{\frac{2i-1}{3}} \beta_{i,(n+1-i)} \tag{2.77}$$

  where $\beta_{i,0} = 1$,

- when $L \leq n$

$$e_n = \left(\sum_{i=1}^{L} \alpha_i d_0^{\frac{2i-1}{3}} \beta_{i,(n+1-i)} \right) - \left(1 + \sum_{i=1}^{L} \alpha_i \right) d_0^{\frac{2L+1}{3}} \beta_{\frac{2L+1}{2},n-L} \tag{2.78}$$

  where $\beta_{\frac{2L+1}{2},0} = 1$.

Chapter 3

Rock-Concrete Interface

3.1 Introduction

Dam safety programs are of utmost importance to society and call for combined use of multidisciplinary efforts. The concept of safety should apply not only to the preplanning stages of design but also to the post-operational and maintenance stages.

Due to this, recent years have witnessed a major research interest from the academic community in fracture mechanics of concrete and a high concern from the engineering community and power utility companies owning dams, in dam safety. From recent studies, it is well understood that the concepts of fracture mechanics could be usefully applied for the failure analysis of concrete dams. In a concrete dam, the interface between the concrete superstructure and the rock foundation is one of the potential sites of crack formation and subsequent failure.

Not only do they contribute in weakening the mechanical strength, but they also constitute conduits for water to seep through and exert uplift pressure. Hence, it is important that proper mechanical behavior of this interface is understood in light of realistic loading conditions.The fracture mode at an interface of dissimilar materials is often mixed. Differences between elastic properties across an interface will generally disrupt the

symmetry even when the geometry and loading are otherwise symmetric with respect to the crack. Mixed mode crack propagation involves the presence of in-plane normal and shearing tractions near the front of an existing crack (notch). The stress and displacement fields near the tip of a crack present between dissimilar materials are given in this thesis.

Figure 3.1. An Example of Gravity Dam Dworshak,Idaho

The Federal Energy RegulationCommission (FERC) guidelines for the evaluation of hydroelectric projects include provisions addressing the use of finite element analysis instead of hand calculation methods.Therefore, besides theoretical considerations, valid fracture mechanics material properties should be determined for dam concrete-rock foundation interface for the use in fracture mechanics-based finite element models. Hence, it is vitally important to conduct experiments on interface specimens to extract valid material properties.

Further, the fracture parameter obtained in the wedge-splitting tests and their numerical analysis is used in the analysis of the Greyrock gravity dam for determining the crack length at the dam-foundation interface.

3.2 Numerical results

Figure 3.2 show a gravity dam model proposed as a benchmark by the Int. Commission On Large Dams [60],[61] (dam height 80 m, base 60 m, $w_{eff,c} = 2.56mm$, $\mu_f \sigma_u = 0.95\ MPa$). Therefore a large value $\mu_f = 45$ is considered.

3.2.1 The Water Lag

As assumed in [73], the water penetrates into the crack where $w > w_{eff,c} * 2/9$. The Figure 4.8 shows the contour lines of τ_{xy} on a deformed mesh. The well established literature on water driven fracture assumes that the water penetrates into the crack but does not reach the FCT. The fraction of FPZ not reached by the water is called water lag. According to the experimental results of Reich et all. [1994], it is assumed that the water penetrates into the FPZ up to the conventional knee point of the softening law ($w > w_{eff,c} \times 2/9 = 2.56 \times 2/9 = 0.569\ mm$). At the points where the water penetrates, the pressure is the same as in the reservoir at the same depth. The concrete and the rock are assumed to be impervious. The asymptotic expansion used is based on the assumption $\tau_{xy}|_{\vartheta=\pi} = -\mu_f\ \sigma_y|_{\vartheta=-\pi}$ therefore it can be applied only in the region not reached by the water. The free parameters of the expansion are calibrated in this region. In the remaining part of the FPZ ordinary shape functions are used. For example, when the distance of the FCT from upstream edge is 12 m Figures 3.4, 3.5 show that the total solution perfectly fits the asymptotic curve in terms of crack opening and sliding displacement.Figures 3.6, 3.7 and 3.8 show the angular distribution of stresses.

3.2.2 The iterative solution procedure

For each position of the fictitious crack tip (shortening FCT) the following iterative procedure is applied:

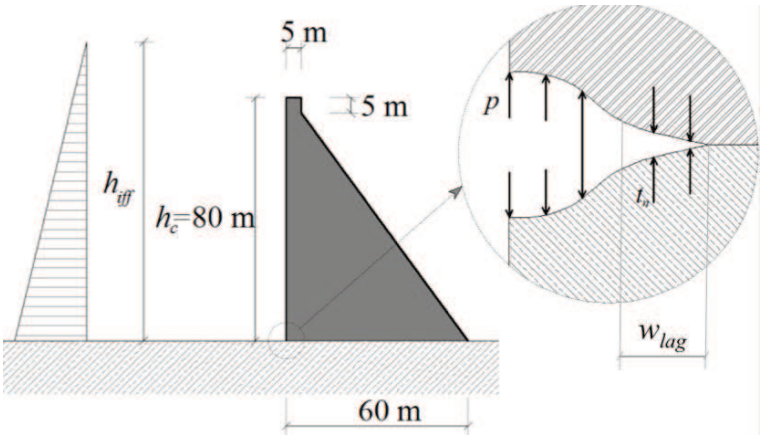

Figure 3.2. Gravity dam proposed as benchmark by ICOLD [60]

$$\begin{bmatrix} w \\ \delta \end{bmatrix}^{i+1} = f\left(\begin{bmatrix} \sigma_y \\ \tau_{xy} \end{bmatrix}^{i} \right), \qquad \begin{bmatrix} \sigma_y \\ \tau_{xy} \end{bmatrix}^{i+1} = g\left(\begin{bmatrix} w \\ \delta \end{bmatrix}^{i+1} \right) \quad i = 0,1,2\ldots \tag{3.1}$$

Since the material outside the fracture process zone (shortening FPZ) is linear, it is possible to compute the overtopping water height (h_{ovt}) and the tangential stress at the FCT ($\tau_{xy,FCT}$) by imposing that the stress field is not singular (stress intensity factors $K_1 = K_2 = 0$). All these linear constraints are included in the operator f.

Since w,δ,σ_y,τ_{xy} are compatible with the asymptotic solution, operator g includes the constraints previously described .

At the first iteration ($i = 0$) $w = \delta = 0$ is assumed along the FPZ. According to this approach h_{ovt} and $\tau_{xy,FCT}$ are not defined *a priori* but are obtained from the analysis related to a pre-defined position of the FCT. The cohesive tractions are applied to the FPZ by writing an user subroutine UTRACLOAD in the framework of abaqus standard code [71].

3.2.3 Comparison between the results based on two different asymptotic expansions

The results obtained through the asymptotic expansion proposed by Karihaloo and Xiao [56] for a crack between similar media are based on the mean values of the elastic properties shown in Table 3.1 (Young's modulus 32500 MPa, Poisson's ratio 0.125). In order to facilitate the comparison with the results based on the expansion proposed in this paper the same position of the fictitious crack tip (12 m from upstream edge) and the same length of the water lag (6.48 m see Figure 3.2) is assumed in both cases. Table 3.2 shows tha main results. Since an increment of water penetration always increases the stress level at the fictitious crack tip it is possible to conclude that the solution obtained through the bi-material model is more conservative. In fact this model predicts the same stress level (see Figure 3.6) for a lower overtopping water height and for a larger COD in comparison to the case of similar media.

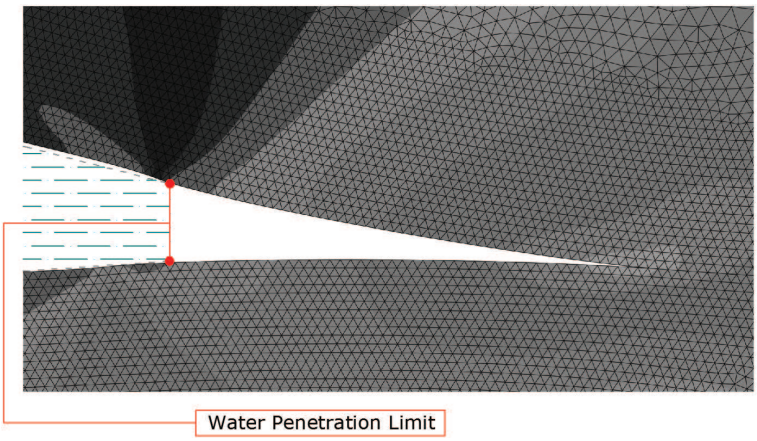

Figure 3.3. Contour lines of τ_{xy} on a deformed mesh

	Density [kg/m^3]	Young's modulus [MPa]	Poisson's ratio [-]
Rock	2700	41000	0.10
Concrete	2400	24000	0.15

Table 3.1. Material Properties.

	Monomaterial	Bi-material
max τ	0.95 MPa	0.975 MPa
max σ_x	2 MPa	2 MPa
Overtopping water height	4.91 m	3.65 m
COD at 6.48m from FCT	0.545 mm	0.608 mm

Table 3.2. Comparison between the main results.

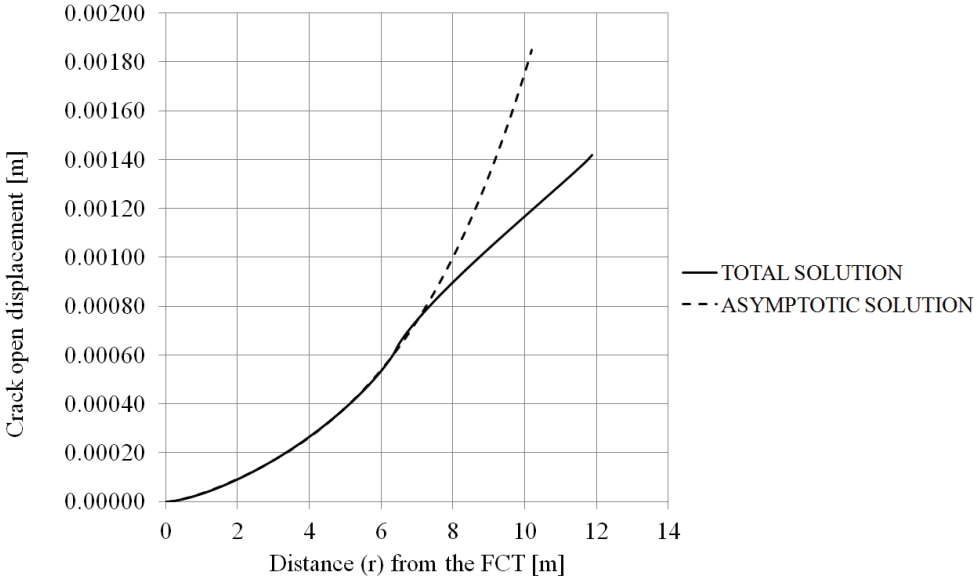

Figure 3.4. Crack opening displacement vs. distance r

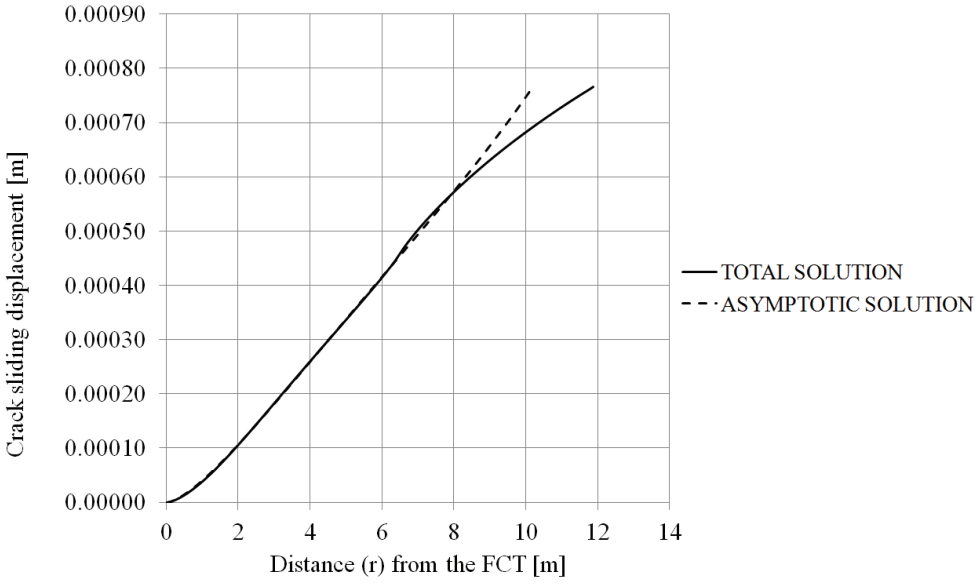

Figure 3.5. Crack sliding displacement vs. distance r

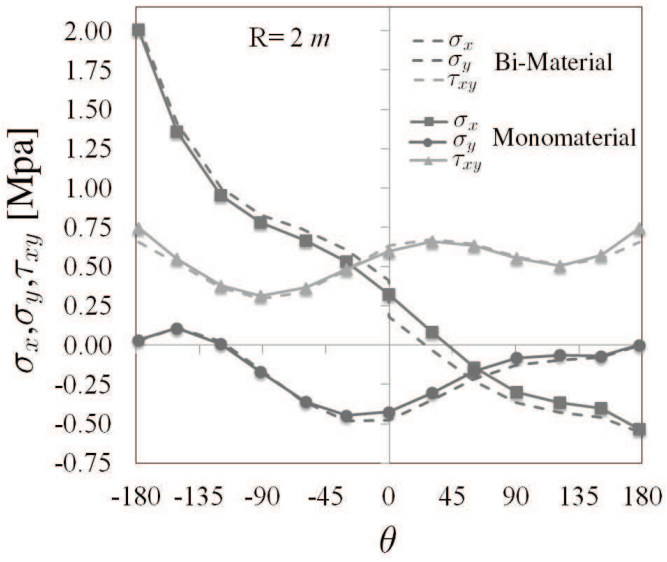

Figure 3.6. Comparison between the monomaterial case and bi-material case

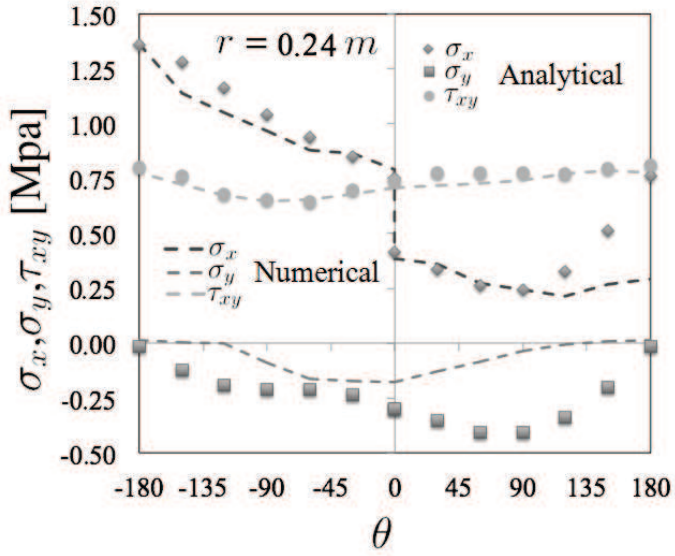

Figure 3.7. Comparison between an analytical ($\lambda \leq 3.5$) and numerical solution in the bi-material case (r=0.24 m)

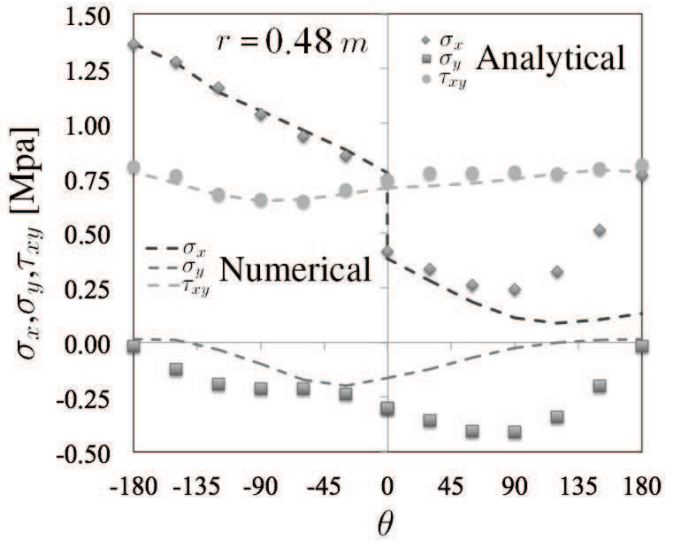

Figure 3.8. Comparison between an analytical ($\lambda \leq 3.5$) and numerical solution in the bi-material case (r=0.48 m)

Chapter 4

Brick-mortar and stone-mortar interfaces

4.1 Introduction

A laboratory procedure aimed at generating a progressive deterioration of the interface between brick and mortar layers in controlled experimental conditions was developed at the Non Destructive Testing Laboratory of the Politecnico di Torino. It is intended as a preliminary stage in the design of a pre-qualification procedure to be applied to repair mortars for restoration of historical masonry buildings. Indeed, assessing the durability of repair products is a major concern because of the potential occurrence of de-bonding phenomena due to insufficient compatibility between original and repair materials, in terms of their mechanical characteristics. Therefore, the study of the long-term mechanical interaction between repair mortars and historical masonry substrate turns out to be crucial for the design of durable repair works. In this direction the evolutionary phenomenon of mortar de-bonding generated in the lab is analyzed here through the cohesive crack model. The numerical simulation of the laboratory tests was shown to be able to describe the experimental evidence correctly, thus allowing us to characterize the mechanical behavior of the interface. It is

therefore possible to use the analysis presented here to predict de-bonding phenomena in problems with different boundary conditions by changing the simulation parameters properly. The laboratory procedure here described was defined in order to create a progressive deterioration at the interface between brick and mortar in a bi-material system, in such a way to simulate a realistic de-bonding phenomenon in an accelerated time frame. It consists in the application of static loads to mixed brick-mortar specimens having peculiar characteristics in terms of geometry and adhesion at the interface (as described in Section 2), with continuous monitoring of the longitudinal and transverse displacements. A numerical simulation based on the cohesive crack model was used to follow the experimental data, so as to describe the evolutionary phenomenon of de-bonding as a function of a small number of parameters and identify potential precursors of the interface failure, that could be used in the future in the framework of a pre-qualification procedure aimed at characterizing the long-term compatibility between restoration materials and original historical materials.

4.2 Brick-mortar interface

The laboratory procedure here described was defined in order to create a progressive deterioration at the interface between brick and mortar in a bi-material system, in such a way to simulate a realistic de-bonding phenomenon in an accelerated time frame. It consists in the application of static loads to mixed brick-mortar specimens having peculiar characteristics in terms of geometry and adhesion at the interface (as described in Section 2), with continuous monitoring of the longitudinal and transverse displacements.

A numerical simulation based on the cohesive crack model was used to follow the experimental data, so as to describe the evolutionary phenomenon of de-bonding as a function of a small number of parameters and identify potential precursors of the interface failure, that could be used in

the future in the framework of a prequalification procedure aimed at characterizing the long-term compatibility between restoration materials and original historical materials.

Figure 4.1. Interface between brick and mortar

4.2.1 Experimental tests

The static compressive tests were performed with the aid of a 250 kN MTS operating in displacement control. The velocity of the machine piston was 0.001 mm/s. Two teflon leaves, 1 mm thick, were located below the specimen in order to reduce friction related to the horizontal expansion. The experimental setup is shown in Figure 4.2.

4.2.2 Loading machine

The new techniques that are currently available have enlarged the field of materials that can be used in construction. It is therefore often necessary to resort to studies on high strength materials, which, at the same time, are brittle and have a tendency to fracture. Electronic or digital servo-controlled test machines have been set up and built in order to be able to

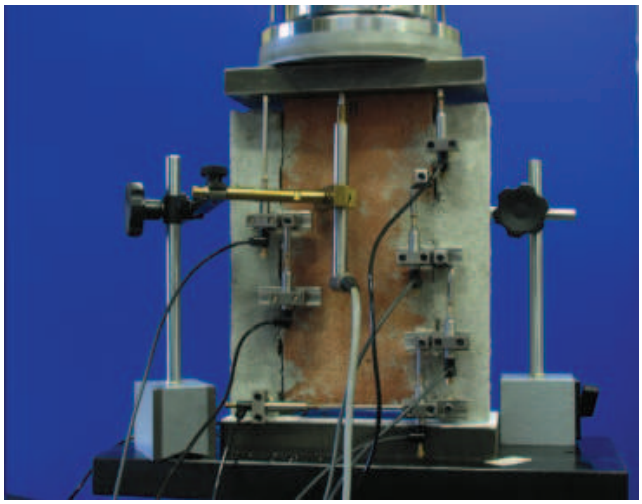

Figure 4.2. Experimental setup

investigate their behavior.

Functioning principle

Servo-driven machines are based on a closed ring or close-loop regulation circuit. Once a physical magnitude has been chosen as the control variable, the variation in time laws are defined, through an electronic system, for this magnitude. A regulation system carries out continuous verifications between the fixed magnitude value, which constitutes the imposed signal, and the magnitude value on the tested element, which, measured by means of a specific transducer, is the signal that is activated by the machine. Any difference between the two signals constitutes an "error" signal which, opportunely amplified, operates a double-acting cylinder, through a hydraulic regulation solenoid (which can be considered the "heart" of the machine), by means of the introduction or removal of oil in the loading piston.

This process, through which the exiting signal of a given failure is brought back to the entrance, is known as feedback. This action has the purpose of guaranteeing an automatic pre-established control. Depending on what type of failure is used in the reaction, it is possible to have a positive reaction, feedback, or a negative reaction, negative feedback.The

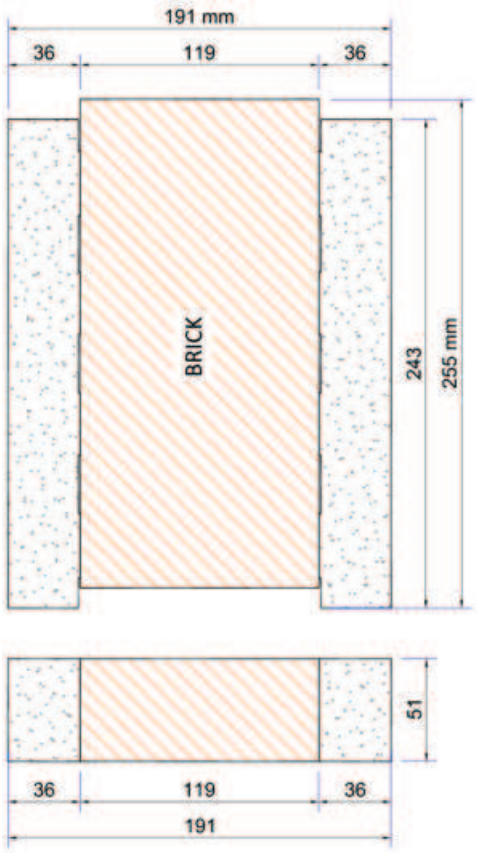

Figure 4.3. Geometry of specimen

former supplies the reactivated system with a higher gain than that of the system without regulation; the latter supplies a lower total gain, but guarantees elevated stability.

Composition

These test machines are made up of three subgroups:

- The loading scaffolding which is foreseen for the application of axial loads of a monotonic type or a dynamic type, and which allows traction and compression tests to be carried out. Its elevated stiffness allows the operator to work with cyclic loads, without any risk of

resonance, and to reduce the losses of power, due to structure strain, to a minimum. The positioning of the upper crosspiece and its attachment are conducted by means of hydraulic devices. This makes it possible to obtain the best possible axial alignment. The axial load is applied by means of a linear, double-acting actuator (hydraulic jack), with a stem loop, incorporated in the base by means of the scaffolding. A four-way solenoid valve allows the flow of oil from the actuator to be regulated, in response to an electric command signal generated by the servo-regulator. There are measurement transducers on the machine that are used to operate the system: an electric strain gauge loading cell (which measures the axial loads), a differential type displacement transducer (LVDT) located inside the actuator (to measure the stroke), a leaf spring type of electric strain gauge to measure the strains on the tested object.

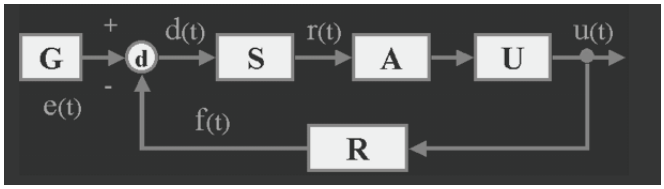

Figure 4.4. Negative feedback process

- The electronic control board which contains the electronic programming, operation and data reading apparatus. Programming takes place through a digital function generator. This unit allows a signal of different shapes to be generated: a ramp with a variable rise time and a sine with different frequency values to carry out cyclic tests. A stopping device which allows the rise or the execution of the loading cycles to be stopped at any given moment and to keep the reached load constant for an indeterminate time. Finally, the ramp rise face can be changed automatically during the test, allowing a different loading velocity or a different frequency and size of the load to be

introduced for the cyclic tests. A command panel allows the programming unit and the hydraulic generator unit, but also the safety devices, to be started and stopped. The servo-regulator includes the negative feedback selector, which allows the desired control magnitude to be chosen. Each transducer has its own supply, amplification and signal conditioning unit.

- The hydraulic generator which supplies a flow of oil to the servo-valve/actuator sub-group. Coupled to a suitable accumulator, it supplies the necessary flow for the functioning of the sine cycle of the servo-valve.

This type of machine was created because of the necessity of operating experimental tests with particular requirements, for example, under the control of one of the following parameters:

- Load applied to the sample
- Deformation of the sample
- Displacement of the loading piston.

It is clear that a greater variety of tests can be carried out with this kind of machine: ranging from the monotonic loading conditions to cyclic loading conditions, conducted on structures made of "softening" materials, such as concrete. In the particular case of Mode 1 type tests, the crack mouth opening displacement (CMOD) can be controlled; without this control, it would not be possible to obtain the descending part of the load-displacement curve: sudden rupture would occur.

The machine in our laboratory and on which the tests have been conducted is an MTS which began to be used in 1993. The loading cylinder can develop a maximum force of 250 kN (both in traction and in compression) and cover a stroke of 80 mm. The electric command unit is an analogue Micro Console 458.20 with 3 signal amplification and conditioning units: piston displacement, loading and strain. Each unit has 4 cartridges which allow the same number of work scales to be chosen:

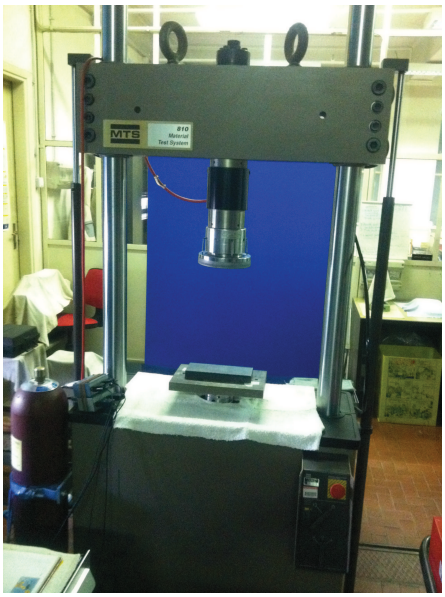

Figure 4.5. Loading machine used in the tests.

- Piston displacement: $\pm 10\ mm$, $\pm 20\ mm$, $\pm 50\ mm$, $\pm 100\ mm$.

- Loading: 25, 50, 125, 250 kN.

The frame of the machine is made up of two 2000 mm high columns which allow an axial work space of 1500 mm to be obtained. It is supplied with a hydraulic lifting and blockage system of the mobile crossbeam. A support plate is supplied for the samples, together with a spherical 165 mm diameter coupling joint. The machine is also supplied with a three point test system for bending tests. It also has a support base with a work space that can be varied up to 1000 mm, which is supplied with a balancing support and a load distributor with a joint. The machine is a 0.5 class machine (UNI EN 10002/2) and is regularly calibrated by the internal calibration group of the Department.

4.2.3 Preparation and packaging of specimens

The geometry of the specimens is shown in Figure 4.3 The external layers of repair mortar were not applied in complete adhesion to the brick support, on the contrary they were applied in symmetrical and regular discontinuity, created in the casting phase through the interposition of a thin steel leaf.

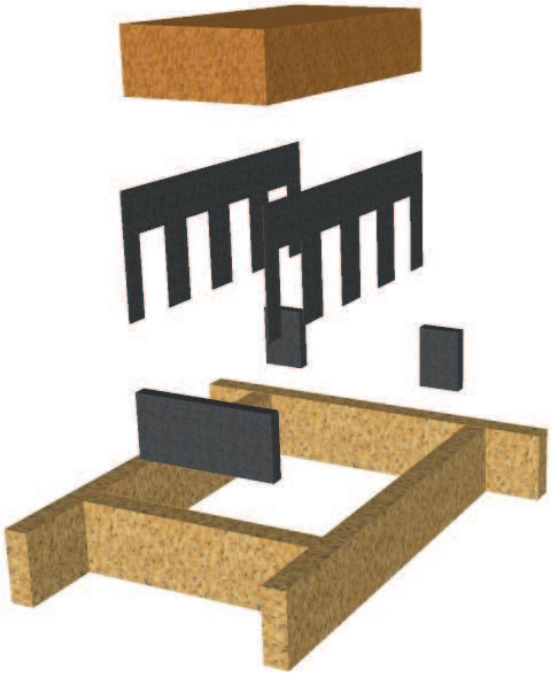

Figure 4.6. Phases of the preparation

These discontinuities, shown in Figure 4.3, behave as notches which are able to trigger multiple crack propagations. The mortar was prepared by mixing cement, sand and water in proportions 1:3:0.5. Specimens were instrumented with seven transducers and tested 28 days after the cast.

The mean value of the mortar compressive strength, evaluated after debonding test, was 36.8 N/mm^2 and the mean value of the Young's modulus was 19500 N/mm^2. The elastic properties of brick and mortar are reported in Table 4.2.

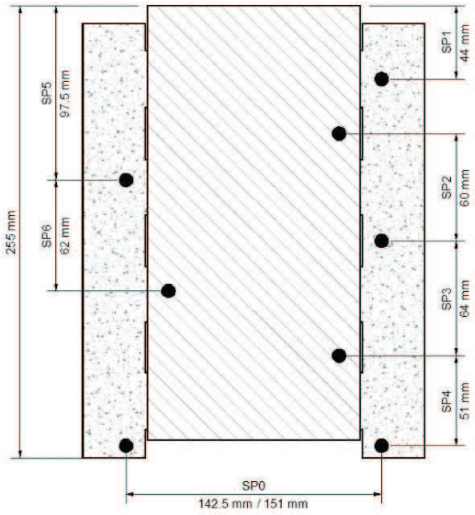

Figure 4.7. Position of transductors

Figure 4.8. Loading machine with specimen before to start the test

4.2.4 Numerical simulation through the cohesive crack model Brick-mortar interface

The method use for the numerical simulation of mortar and brick fracture is the cohesive crack modell, also known as Barenblatt ,Dugdale and Hillerborg model for quasi-brittle materials. In this case the crack initiation criterion is assumed as:

$$\left(\frac{\sigma_0}{f_t}\right)^2+\left(\frac{\tau_0}{f_s}\right)^2=1 \tag{4.1}$$

where σ_0 and τ_0 are stresses evaluated along the directions normal and tangential to the interface and ft and fs are the related strength. The point where Eq.(4.1) is satisfied is called fictitious crack tip. According to this method the cohesive stresses acting on the non-linear fracture process zone (shortened FPZ) are decreasing functions of the effective value of the displacement discontinuity (see [41],[73]). In this case it was assumed:

$$w_{eff}=\sqrt{\left(\frac{w_n}{w_{nc}}\right)^2+\left(\frac{w_t}{w_{tc}}\right)^2} \tag{4.2}$$

where w_n is the mutual displacement component normal to the interface and w_t the tangential one. w_{nc} e w_{tc} are the related critical values. If $w_{eff} > 1$ no stress transfer occurs and therefore the crack is stress free. Otherwise the stresses are decreasing functions of w_{eff} following a predefined softening law. In the present work the above mentioned law is linear, starting from σ_0 and τ_0 and ending in the point where $w_{eff} = 1$ called real crack tip. The behavior of the material outside the FPZ is linear elastic. In a symmetric model, it is well known that the fracture process starts symmetrically, but loses this property before the peak load is reached. In order to simulate numerically this experimental evidence, a realistic scatter in strength was assumed, as shown in Table 4.1.

Therefore the collapse is determined by a de-bonding process occurring on the right (weaker) side.Table 4.2 shows the elastic properties assumed.

	f_t [N/mm^2]	f_s [N/mm^2]	w_{nc} [mm]	w_{tc} [mm]
left side	1.5	1.5	0.01	0.01
right side	1.3	1.3	0.01	0.01

Table 4.1. Interface parameters Brick-Mortar interfaces

	Young's module [N/mm^2]	Poisson ratio [-]
Mortar	19500	0.15
Brick	14500	0.20

Table 4.2. Elastic Properties

The numerical analysis were executed through the code ABAQUS [45] by applying a pre-defined downward velocity to the upper face of the stone block. The deformed finite element mesh shown in Figure 4.9.

Time values are normalized by assuming the value $T = 1000s$ at peak load. Table 4.3 shows that the maximum value of displacements, evaluated experimentally, is always larger than the same value, obtained numerically. The numerical analysis have to be arrested as soon as uniqueness of incremental solution is lost in the model.

	Load Max [N]	Max V displ. [mm]	Max H disp. [mm]
Specimen 1	8655	0.32	1.60
Specimen 2	5809	0.37	1.14
Numerical Results	7497	0.019	0.042

Table 4.3. Maximum values of load and displacement (Brick-mortar case)

On the contrary the experimental test can be executed up the complete plaster de-bonding. With reference to the vertical displacement, it's worthwhile noting that experimental values include the deformation of the teflon leaves. On the contrary, in the numerical simulation, this contribution is

Figure 4.9. Finite element mesh at the end of the fracture process. Displacements are enlarged 781 times

neglected.

All diagrams start when the external load exceeds 10% of the maximum value. The vertical displacement achieved at this time was assumed as zero. In this way the effects of local settlements occurring at the supports are reduced on the experimental diagrams. The numerical diagrams are not sensible to local support settlements and therefore starts linearly from the origin.

In Figures 4.10 and 4.11 symbol (□) indicates the global horizontal displacement evaluated from the mortar on the left side to the mortar on the right. In both cases this diagram shows a knee point: on the left there are small values due to elastic deformation, on the right large values due to the non-linear fracture process. The above mentioned knee point occurs

at the time of the peak-load. It means that the crack growing from the bottom to the top causes the global softening branch. Figure 4.16 shows the same diagrams obtained through the cohesive crack model. Numerical and experimental results are in good agreement.

In Figures 4.10 , 4.11 and 4.16 symbol (△) indicates the vertical displacement of the loading point. Since this is the control parameter, the numerical response is perfectly linear. From the experimental point of view, a constant velocity of the machine piston was enforced. Therefore small deviations from the linear diagram are due to the elastic global behavior of the testing machine.

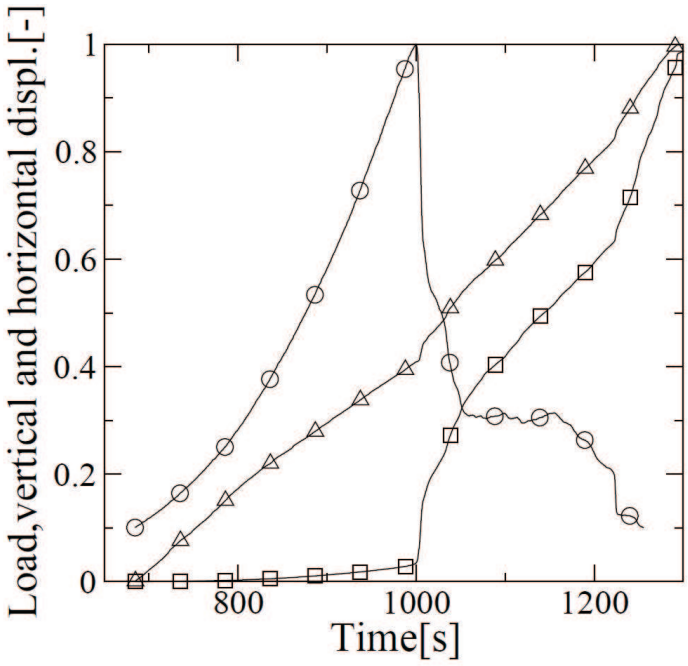

Figure 4.10. Dimensionless experimental results for the first specimen

The simbol (◯) represents the load and the symbol (□) represent mortar to mortar horizontal displacement at specimen bottom.

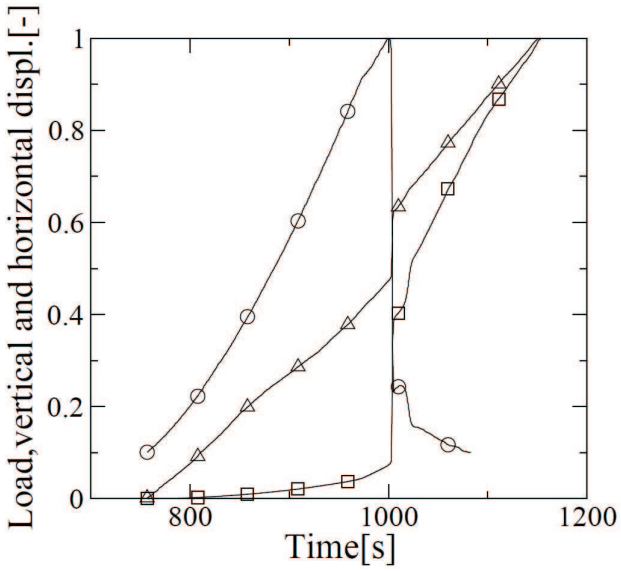

Figure 4.11. Dimensionless experimental results for the second specimen

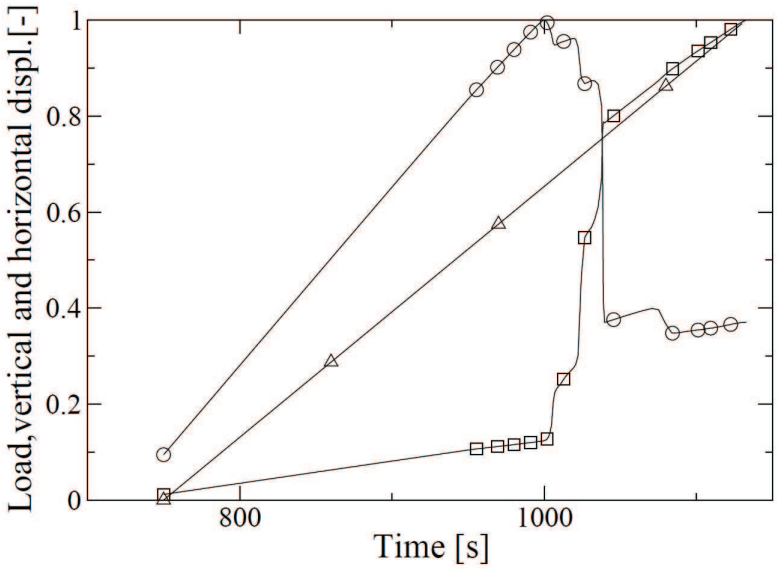

Figure 4.12. Dimensionless numerical results

The insertion of the Teflon ,Figure 4.13, improves the conditions of stability of the experimental evidence. The lower curve represents the curve load - displacement in the case that there is Teflon. It can be seen that the maximum load is decrease considerably, with two immediate consequences: test less brittle and decrease of the peaks in the initial of the test.

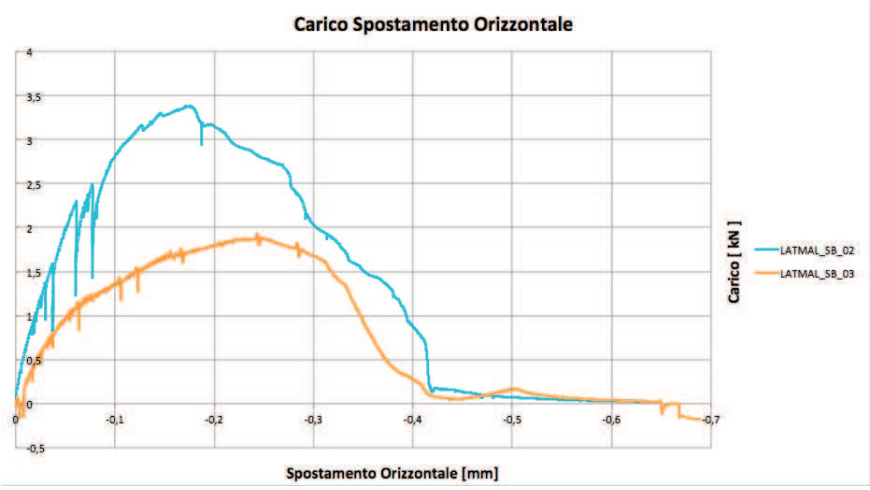

Figure 4.13. Comparison Specimen with and without teflon

4.3 Stone-mortar interface

Often masonry walls of historical buildings are subjected to rising damp effects by capillary action or by rain infiltrations. The decay and delamination of plasters occur frequently as a consequence of damp actions. The restoration market offers a lot of dehumidified repair mortars to put the new transpiring plasters, whose mechanical characteristics however are not compared carefully with those of historical masonry support. The goal of this experimental and numerical analisys is to focus one's attention on the preliminary pre-qualification of repair materials before their use, in order to avoid any mechanical and phisycs incompatibility and in the maintime to guarantee the maximum durability of restoration work [43].

Figure 4.14. The Transfiguration Chapel of the Sacri Monti di Varallo

This experimental study is carrying out in the UNESCO heritage site of the Sacri Monti di Varallo Figure 4.14. Situated at the top of the hill above the town of Varallo in Piedmont (Italy), the Sacro Monte is an artistic-religious complex consisting in 45 chapels, populated with frescoes and sculptures wich tell the story of the life of Christ. The aim of this particular architectural site was to reproduce the holy sites of Palestine where the earthly life of Christ had taken place. Realised between the 15th and the 18th centuries by the major artists of Piedmont and Lombardy of the period, the Sacro Monte is also a beautiful example of park gardens. The chapels were constructed very simply sometimes making use of natural materials, stone or brick walls, wood roofs with stone surface. Because of the capillary action, of the freeze-thaw cycles and of the abundant rain and snow precipitations that characterize this mountain area, for a long time

the historical plasters of the chapels are subjecting to progressive material decay.

From 2010 a research group of Politecnico di Torino composed by engineers, architects, physicists, chemists, get together around the RE-FRESCOS project, is studying the decay of these plasters in different scientific ways, through sophisticated non destructive tests in situ and in the laboratory. The research aim is to offer appropriate technical answers to stop this decay, to restore the masonry surfaces by means of compatible and durable materials and techniques, in order to save the frescos of the chapels.

Inside this project the research group of the Laboratory non Destructive Testing Materials of the Politecnico di Torino is carrying out particular fatigue tests on ad hoc mixed brick-mortar specimens useful to evaulate the mechanical adhesion of the new repair mortars to masonry support [44]. Unfortunately some recent restoration work on decay plasters have shown already their poor durability because of incompatibility of the employed repair mortars, not suitable for the thermal and mechanics stresses peculiar to the place. The results of this incompatibility were the early delamination and decay of new repair plasters.

4.3.1 Specimen preparation and experimental setup

The geometry of the stone block-mortar specimens is shown in Figure 4.15. Two mixed specimens were tested, manufactured by a stone block (similar to that of the Sacro Monte masonries) joined to symmetrical layers of repair mortar in the two shorter stone vertical sides. The stone surfaces to contact with the mortar are been treated with carvings shown in Figure 4.15 in order to improve the adherence of the strengthening product. The layers of dehumidifying mortar were not applied in complete adherence to the stone block support, on the contrary in symmetrical and regular discontinuity at the bottom and in the top of the specimen. These discontinuities behave as notches which are able to trigger multiple crack propagation. The aim of this particular mixed specimens and test is to simulate the adherence capacity of every repair mortar applied to a specific masonry wall

for dehumidified plaster.

Figure 4.15. Specimen preparation

The pre-blended mortar, chosen among the principal ones on the market, is a transpirant base render made from natural hydraulic lime and Eco-Pozzolan, suitable for the restoration of old historical masonry damaged by rising capillary damp and sulphate salts. The Young's modulus of this repair mortar, evaluated according to UNI6556, was 4379 MPa. The compressive strength, evaluated according to UNI6556, was 33,8 MPa. The above mentioned values were evaluated 28 days after the cast. The mixed pieces were instrumented with two symmetrical couple of inductive displacement transducers shown in Figure 4.16. One transducer (SP0), one for side, was arranged horizontally in the low part of the specimen and connected among the two opposite mortar layers, in order to measure the displacements due to bulging. The other transducers (SPV), one for side, have been placed vertically on the stone block.

The static compressive tests were performed with the aid of a 250 kN servo controlled machine, model 810 MTS. Tests of monotonous compression are carried out by the control of horizontal opening (SPO transducers)

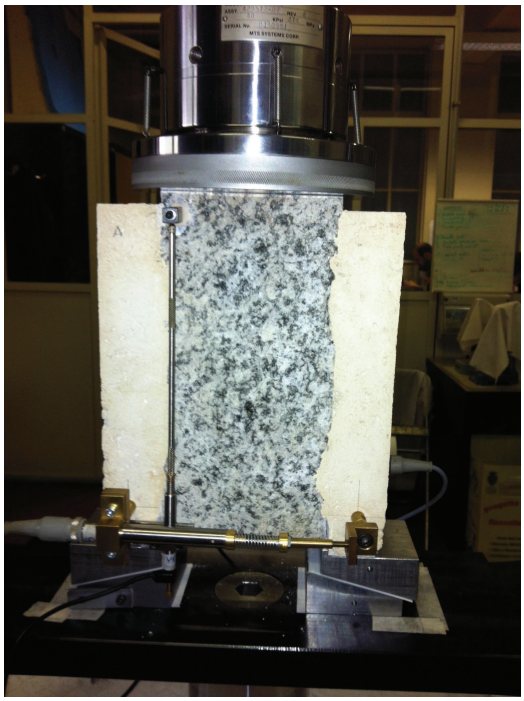

Figure 4.16. Herringbone and Bushhammering Hand

with a speed opening 0,0001 mm /s. The specimens were subjected to static tests after 28 days of maturation. The inferior support of the mortars layers was constituted from a double systems of steel wedges, shown in Figure 4.18, coupled with and without teflon, and inclination angle of 15 gradi.

The mixed specimens were labelled with "SM" (Stone block-Mortar), following by the number order. The two static tests represent the first step of this experimental study, currently in progress. The following step will concern the same type of mixed specimens subjected to cyclic fatigue tests.

Figure 4.17. Herringbone and Bushhammering Hand

4.3.2 Numerical simulation through the cohesive crack model

The method use for the numerical simulation of mortar and stone fracture is the cohesive crack modell, also known as Barenblatt ,Dugdale and Hillerborg model for quasi-brittle materials,and the model is the same that we used in Capter 4.2.4. In the present work the above mentioned law is exponential, starting from σ_0 and τ_0 and ending in the point where $w_{eff} = 1$ called real crack tip. It is assumed as follows:

$$\frac{\sigma}{\sigma_0} = \frac{\tau}{\tau_0} = \left[1 - \frac{1 - exp(-\alpha\ w_{eff})}{1 - exp(-\alpha)}\right] \tag{4.3}$$

The behavior of the material outside the FPZ is linear elastic. In a symmetric model, it is well known (see [46], [74] and [75]) that the fracture process starts symmetrically, but loses this property before the peak load is reached. In order to simulate numerically this experimental evidence, a realistic scatter in strength was assumed, as shown in Table 4.4.

Therefore the collapse is determined by a de-bonding process occurring

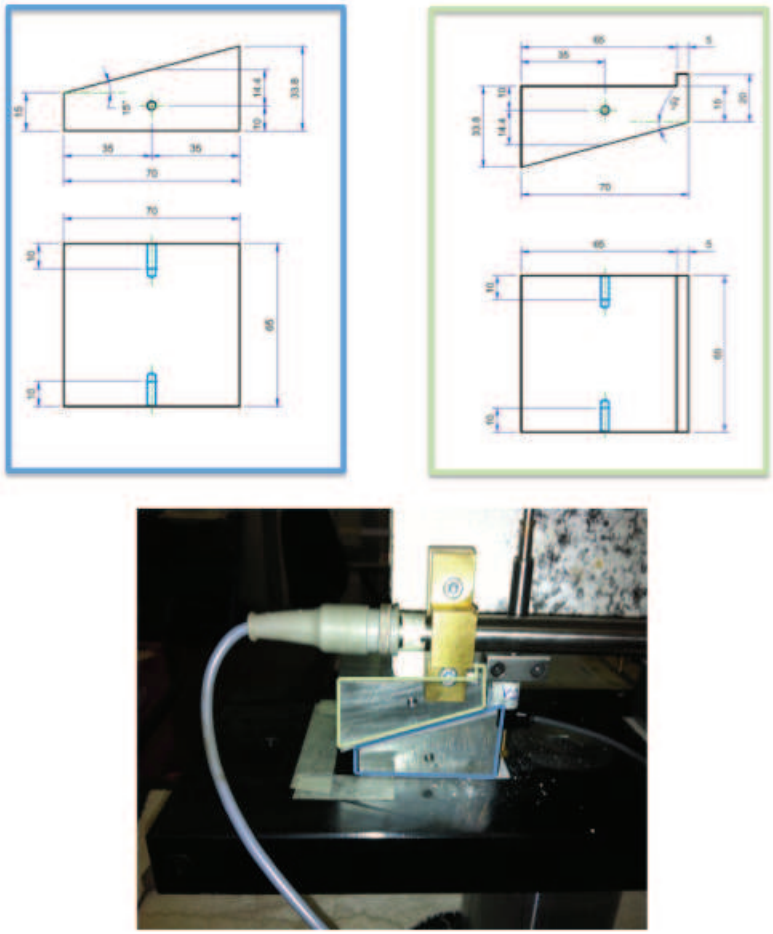

Figure 4.18. Position of steel wedges

	f_t [N/mm^2]	f_s [N/mm^2]	w_{nc} [mm]	w_{tc} [mm]
left side	0.242255	0.361	0.5	0.5
right side	0.232751	0.3515	0.5	0.5

Table 4.4. Interface parameters

on the right (weaker) side.Table 4.2 shows the elastic properties assumed.

	Young's module [N/mm^2]	Poisson ratio [-]
Mortar	4180	0.15
Stone	23750	0.20

Table 4.5. Elastic Properties

The numerical analysis were executed through the code ABAQUS [45] by applying a pre-defined downward velocity to the upper face of the stone block. The deformed finite element mesh shown in Figure 4.19 .

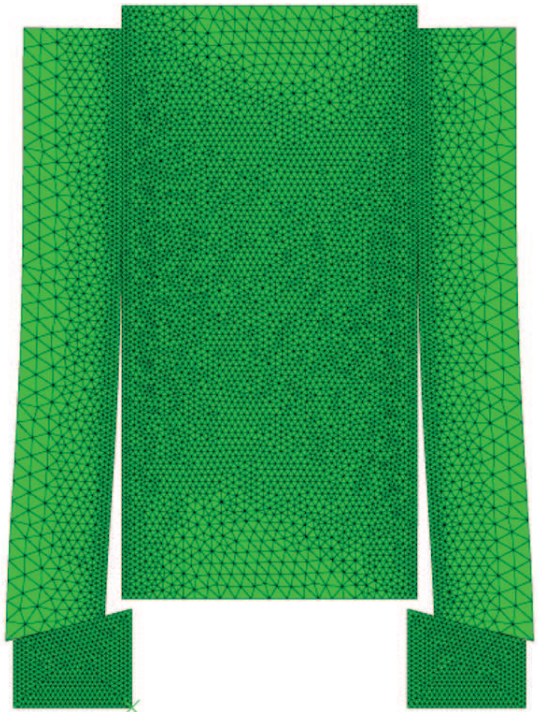

Figure 4.19. Deformed Mesh

A preliminary elastic analysis shows four points of stress singularities: two notch tips on the specimen top, and two on the specimen bottom (see

Figure 4.19). From this points, four cohesive cracks start to propagate along the bi-material interfaces, which are the weakest planes involved into the singular stress fields. Because of the wedges (see Figure 4.19), the cracks starting from the specimen bottom show a growing velocity larger than the cracks starting from the specimen top. Therefore the second couple of cracks plays the role of main cracks. The surface treatment shown in Figure 4.17 increases the values of w_{nc} and w_{tc} in comparison to the case of the interface between the same type of mortar and brick discussed in [77]. Therefore the loss of simmetry does not occurs any longer at the peak load, but it occurs at the end of the softening phase and it causes the specimen collapse.

Figure 4.20 show that the teflon sheet, inserted at the contact surface between upper and lower wedge, is able to reduce the friction and therefore it reduces the load values too. In the numerical simulation the friction is disregarded. Numerical and experimental results are in good agreement.

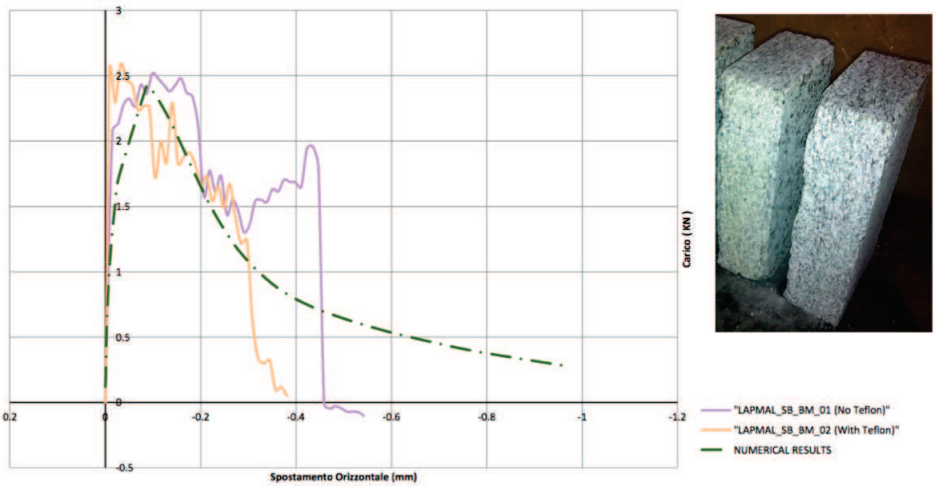

Figure 4.20. Load-horizontal displacement (Hand hammered surface)

Figure 4.21 show that the teflon sheet, inserted at the contact surface between upper and lower wedge, is able to reduce the friction and therefore it reduces the load values too. In the numerical simulation the friction is

disregarded. Numerical and experimental results are in good agreement.

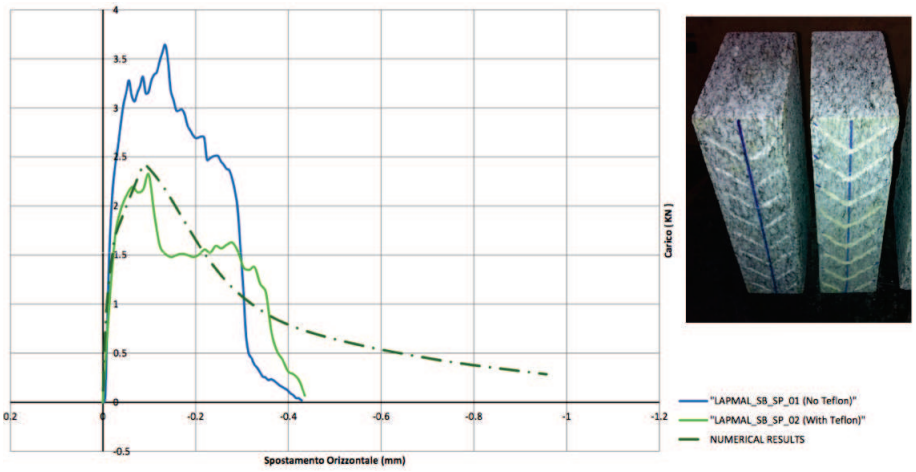

Figure 4.21. Load-horizontal displacement (Surface herringbone)

Figure 4.22 show that the teflon sheet, inserted at the contact surface between upper and lower wedge, is able to reduce the friction and therefore it reduces the load values too. In the numerical simulation the friction is disregarded. Numerical and experimental results are in good agreement.

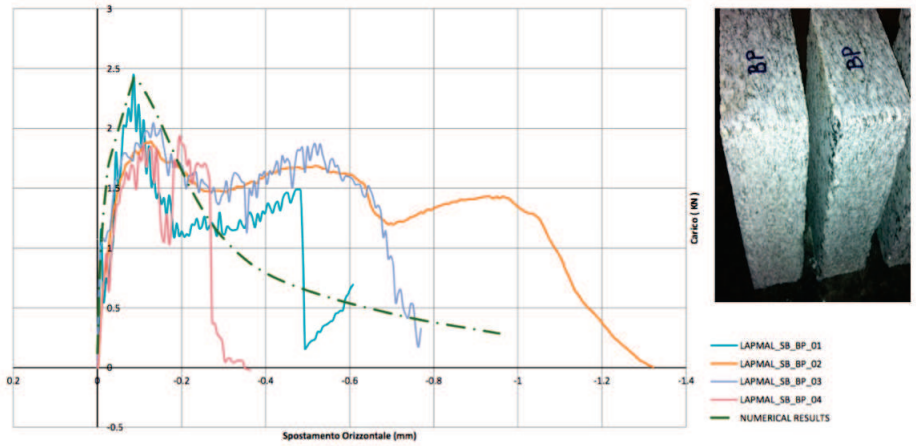

Figure 4.22. Load-horizontal displacement (Pneumatic hammered surface)

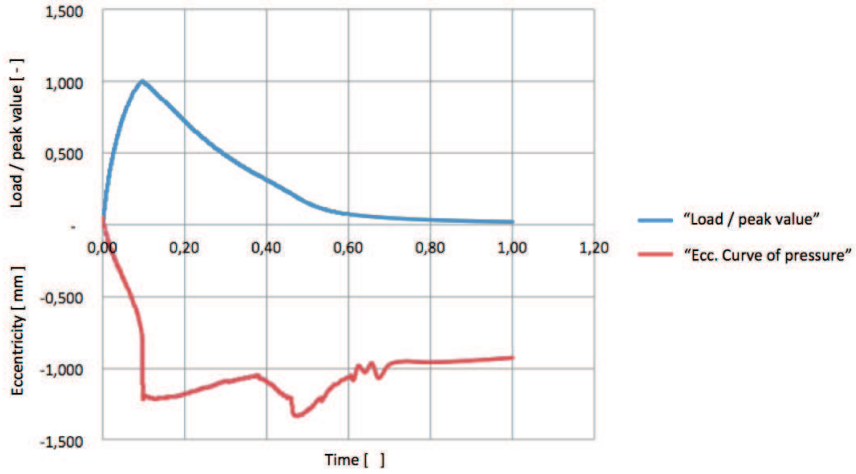

Figure 4.23. Vertical reaction eccentricity vs conventional time and Dimensionless reaction vs conventional time.

As a consequence of the strength scatter assumed, of the mesh chosen and of round off errors an eccentricity appears on the vertical downwards reaction applied to the specimen (see Figure 4.23) during the numerical simulation. Figure 4.24 show the horizontal reaction that appears in the same context.

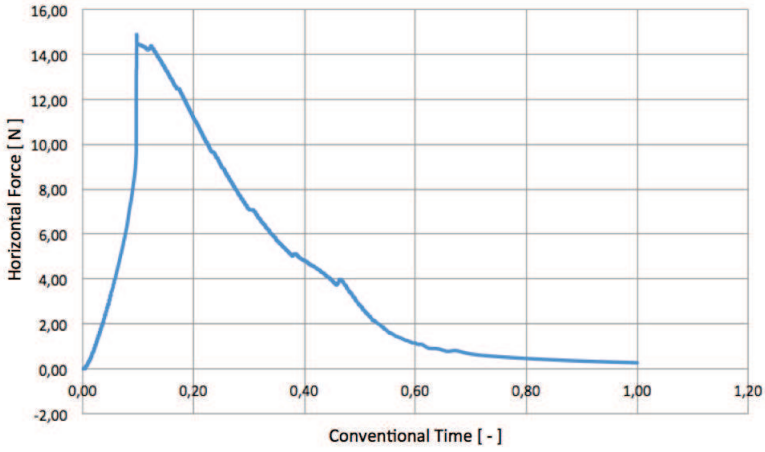

Figure 4.24. Horizontal reaction vs conventional time.

Chapter 5

Conclusions

The reference volume involved in the fracture process of a dam joint is so large that it cannot be tested in a laboratory: a numerical model is needed.

The use of the asymptotic expansions proposed by Karihaloo & Xiao [56] at the tip of a crack with normal cohesion and Coulomb friction can overcome the numerical difficulties that appear in large scale problems when the Newton-Raphson procedure is applied to a set of equilibrium equations based on ordinary shape functions (Standard Finite Element Method).

In this way it is possible to analyze problems with friction and crack propagation under the constant load induced by hydro-mechanical coupling.

In the analysis of the dam-foundation joint penetrated by the water, for each position of the FCT, the condition $K_1 = K_2 = 0$ allows us to obtain the external load level and the tangential stress at the FCT. If the joint strength is larger than the value obtained, the solution is acceptable, because the tensile strength is assumed negligible and the condition $K_1 = 0$ is sufficient to cause the crack growth. Otherwise the load level obtained can be considered as an overestimation of the critical value and a special form of contact problem have to be solved along the FPZ.

For the boundary condition analyzed, after an initial increasing phase, the water lag remains almost constant.

The special polynomial form proposed as a cohesive law can represent most of the commonly used cohesion-separation relations.In this way , the

asymptotic fields can be written in terms of r and θ functions (separable form). Thus the asymptotic fields at the tip of a cohesive crack growing at a bi-material interface are known. The simple assumption of mean elastic values is not conservative.

- An interfacial crack growing between dissimilar media is analysed through the cohesive-frictional crack model.
- An asymptotic expansion for the stress and displacement fields around the fictitious crack tip is obtained.
- The expansion proposed is valid for many commonly used separation laws, e.g. rectangular, linear, bilinear, exponential etc with or without proportional friction on the crack faces.
- The expansion proposed is able to stabilize the equilibrium interations required by the Newton-Raphson method in the numerical simulation of a crack growing at a bi-material interface between a gravity dam and the foundation rock.
- The results obtained through the new asymptotic expansion are compared with the results obtained through the expansion proposed by Karihaloo and Xiao [56] for an interfacial crack between similar media . The assumption of mean values of elastic parameters is not conservative.

For the second part:

An innovative laboratory procedure as a preliminary design stage for the pre-qualification of repair mortars applied to historical stone buildings was described. A numerical simulation based on the cohesive crack model was used to follow the experimental data. The evolutionary phenomena involved in the de-bonding process of mortar in a coupled stone block - mortar system are accurately analyzed by means of the experimental setup proposed. Through the cohesive crack model it was possible to interpret theoretically the above mentioned phenomena occurring at the interface between stone block and mortar. Therefore the mechanical behavior of the

interface is characterized. The parameters obtained can be used for the analysis of a problem with different boundary conditions.

Chapter 6

Appendix

6.1 Appendix A

The problem is to find:

$$\alpha_1,\alpha_2,\ldots,\alpha_5$$

so that the function:

$$f(x) = 1 + \alpha_1\ x^{1/3} + \alpha_2\ x + \alpha_3\ x^{5/3} + \alpha_4\ x^{7/3} + \alpha_5\ x^3 + \\ - (1 + \alpha_1 + \alpha_2 + \alpha_3 + \alpha_4 + \alpha_5)\ x^{11/3}$$

go through a set of n predefined points:

$$(x_i,y_i)\ , \qquad i = 1,\ldots,n$$

i.e.

$$f(x_i) = y_i\ , \qquad i = 1,\ldots,n$$

$$\begin{cases} (x_1^{1/3} - x_1^{11/3})\alpha_1 + (x_1 - x_1^{11/3})\alpha_2 + (x_1^{5/3} - x_1^{11/3})\alpha_3 + \\ \qquad +(x_1^{7/3} - x_1^{11/3})\alpha_4 + (x_1^3 - x_1^{11/3})\alpha_5 = y_1 - 1 + x_1^{11/3} \\ \\ (x_2^{1/3} - x_2^{11/3})\alpha_1 + (x_2 - x_2^{11/3})\alpha_2 + (x_2^{5/3} - x_2^{11/3})\alpha_3 + \\ \qquad +(x_2^{7/3} - x_2^{11/3})\alpha_4 + (x_2^3 - x_2^{11/3})\alpha_5 = y_2 - 1 + x_2^{11/3} \\ \\ \qquad \cdots\cdots\cdots\cdots\cdots \\ \\ (x_n^{1/3} - x_n^{11/3})\alpha_1 + (x_n - x_n^{11/3})\alpha_2 + (x_n^{5/3} - x_n^{11/3})\alpha_3 + \\ \qquad +(x_n^{7/3} - x_n^{11/3})\alpha_4 + (x_n^3 - x_n^{11/3})\alpha_5 = y_n - 1 + x_n^{11/3} \end{cases}$$

in matrix form:

$$A\ z = b$$

where:

$$A = \begin{bmatrix} (x_1^{1/3} - x_1^{11/3}) & (x_1 - x_1^{11/3}) & (x_1^{5/3} - x_1^{11/3}) & (x_1^{7/3} - x_1^{11/3}) & +(x_1^3 - x_1^{11/3}) \\ (x_2^{1/3} - x_2^{11/3}) & (x_2 - x_2^{11/3}) & (x_2^{5/3} - x_2^{11/3}) & (x_2^{7/3} - x_2^{11/3}) & +(x_2^3 - x_2^{11/3}) \\ \cdots & \cdots & \cdots & \cdots & \cdots \\ (x_n^{1/3} - x_n^{11/3}) & (x_n - x_n^{11/3}) & (x_n^{5/3} - x_n^{11/3}) & (x_n^{7/3} - x_n^{11/3}) & +(x_n^3 - x_n^{11/3}) \end{bmatrix}$$

and

$$b = \begin{bmatrix} y_1 - 1 + x_1^{11/3} \\ y_2 - 1 + x_2^{11/3} \\ \cdots \\ y_n - 1 + x_n^{11/3} \end{bmatrix}$$

and z is the unknown vector:

$$z = \begin{bmatrix} \alpha_1 \\ \alpha_2 \\ \cdots \\ \alpha_5 \end{bmatrix}$$

Since the points are more than the unknowns ($n > 5$) the problem usually has no solution.We search the vector z such that the norm of $Az - b$ is

minimal. Such a vector z solves the linear system:

$$A^T \ Az = A^T \ b$$

where A^T is the transpose matrix of A, and solution is (see [39]):

$$z = (A^T A)^{-1} \ A^T \ b$$

```
> restart;
> with(linalg);
```

[*BlockDiagonal*, *GramSchmidt*, *JordanBlock*, *LUdecomp*, *QRdecomp*, *Wronskian*, *addcol*, *addrow*, *adj*, *adjoint*, *angle*, *augment*, *backsub*, *band*, *basis*, *bezout*, *blockmatrix*, *charmat*, *charpoly*, *cholesky*, *col*, *coldim*, *colspace*, *colspan*, *companion*, *concat*, *cond*, *copyinto*, *crossprod*, *curl*, *definite*, *delcols*, *delrows*, *det*, *diag*, *diverge*, *dotprod*, *eigenvals*, *eigenvalues*, *eigenvectors*, *eigenvects*, *entermatrix*, *equal*, *exponential*, *extend*, *ffgausselim*, *fibonacci*, *forwardsub*, *frobenius*, *gausselim*, *gaussjord*, *geneqns*, *genmatrix*, *grad*, *hadamard*, *hermite*, *hessian*, *hilbert*, *htranspose*, *ihermite*, *indexfunc*, *innerprod*, *intbasis*, *inverse*, *ismith*, *issimilar*, *iszero*, *jacobian*, *jordan*, *kernel*, *laplacian*, *leastsqrs*, *linsolve*, *matadd*, *matrix*, *minor*, *minpoly*, *mulcol*, *mulrow*, *multiply*, *norm*, *normalize*, *nullspace*, *orthog*, *permanent*, *pivot*, *potential*, *randmatrix*, *randvector*, *rank*, *ratform*, *row*, *rowdim*, *rowspace*, *rowspan*, *rref*, *scalarmul*, *singularvals*, *smith*, *stackmatrix*, *submatrix*, *subvector*, *sumbasis*, *swapcol*, *swaprow*, *sylvester*, *toeplitz*, *trace*, *transpose*, *vandermonde*, *vecpotent*, *vectdim*, *vector*, *wronskian*] **(1)**

```
> Digits:=16;
```

$$Digits := 16 \quad \textbf{(2)}$$

```
> x1:=0.0015;
```

$$x1 := 0.0015 \quad \textbf{(3)}$$

```
> x2:=0.15;
```

$$x2 := 0.15 \quad \textbf{(4)}$$

```
> x3:=0.24;
```

$$x3 := 0.24 \quad \textbf{(5)}$$

```
> x4:=0.66;
```

$$x4 := 0.66 \quad \textbf{(6)}$$

```
> x5:=0.99;
```

$$x5 := 0.99 \quad \textbf{(7)}$$

```
> y1:=0.97279807608808;
```

$$y1 := 0.97279807608808 \quad \textbf{(8)}$$

```
> y2:=0.381748516040886000;
```

$$y2 := 0.381748516040886000 \quad \textbf{(9)}$$

```
> y3:=0.253701598241544000;
```

$$y3 := 0.253701598241544000 \quad \textbf{(10)}$$

```
> y4:=0.072342811866795000;
```

$$y4 := 0.072342811866795000 \quad \textbf{(11)}$$

```
> y5:=0.001398290719846880;
```

$$y5 := 0.001398290719846880 \quad \textbf{(12)}$$

```
> A:=Matrix([[x1^(1/3)-x1^(11/3),x1-x1^(11/3),x1^(5/3)-x1^(11/3),
  x1^(7/3)-x1^(11/3),x1^3-x1^(11/3)],[x2^(1/3)-x2^(11/3),x2-x2^
  (11/3),x2^(5/3)-x2^(11/3),x2^(7/3)-x2^(11/3),x2^3-x2^(11/3)],[x3^
  (1/3)-x3^(11/3),x3-x3^(11/3),x3^(5/3)-x3^(11/3),x3^(7/3)-x3^
  (11/3),x3^3-x3^(11/3)],[x4^(1/3)-x4^(11/3),x4-x4^(11/3),x4^(5/3)-
  x4^(11/3),x4^(7/3)-x4^(11/3),x4^3-x4^(11/3)],[x5^(1/3)-x5^(11/3),
  x5-x5^(11/3),x5^(5/3)-x5^(11/3),x5^(7/3)-x5^(11/3),x5^3-x5^(11/3)
  ]]);
```

$$A := \begin{bmatrix} [0.1144714242111082, 0.001499999955774989, 0.00001965551623155569, \\ 2.575164795634724\ 10^{-7}, 3.330774988972725\ 10^{-9}], \\ [0.5303764856120635, 0.1490472010207580, 0.04139382232040424, \\ 0.01100210992406233, 0.002422201020757959], \\ [0.6161077310896565, 0.2346612298988847, 0.08734821082102517, \end{bmatrix} \quad \textbf{(13)}$$

Figure 6.1. Extract from Maple

```
    0.03045654836747316, 0.008485229898884710],
    [0.6527233772848546, 0.4420646081674934, 0.2823754250465260,
    0.1613235679950159, 0.0695606081674934],
    [0.0328359827099834, 0.0261804892973870, 0.0195694401213979,
    0.0130025383910727, 0.0064794892973870]]
> b:=Matrix([[y1-1+x1^(11/3)],[y2-1+x2^(11/3)],[y3-1+x3^(11/3)],[y4
  -1+x4^(11/3)],[y5-1+x5^(11/3)]]);
```

$$b := \begin{bmatrix} -0.02720192386769499 \\ -0.6172986849798720 \\ -0.7409596316573407 \\ -0.7097217963006984 \\ -0.0347821985775401 \end{bmatrix} \quad \textbf{(14)}$$

```
> At:=A^+:
> B:=At.A:
> d:=At.b:
> C:=1/B:
> z:=C.d;
```

$$z := \begin{bmatrix} -0.1384712488919 \\ -7.83711782405 \\ 20.9185449918 \\ -25.0792940228 \\ 14.1484129021 \end{bmatrix} \quad \textbf{(15)}$$

Figure 6.2. Extract from Maple

```
> restart;
> with(plots);
```

[animate, animate3d, animatecurve, arrow, changecoords, complexplot, complexplot3d, conformal, conformal3d, contourplot, contourplot3d, coordplot, coordplot3d, densityplot, display, dualaxisplot, fieldplot, fieldplot3d, gradplot, gradplot3d, implicitplot, implicitplot3d, inequal, interactive, interactiveparams, intersectplot, listcontplot, listcontplot3d, listdensityplot, listplot, listplot3d, loglogplot, logplot, matrixplot, multiple, odeplot, pareto, plotcompare, pointplot, pointplot3d, polarplot, polygonplot, polygonplot3d, polyhedra_supported, polyhedraplot, rootlocus, semilogplot, setcolors, setoptions, setoptions3d, spacecurve, sparsematrixplot, surfdata, textplot, textplot3d, tubeplot] (1)

```
> Digits:=16;
```

$$Digits := 16 \tag{2}$$

```
> fk:=(a1,a2,a3,a4,a5,x)->1+a1*x^(2/3)+a2*x^(4/3)+a3*x^(2)+a4*x^
  (8/3)+a5*x^(10/3)-(1+a1+a2+a3+a4+a5)*x^(4);
```

$$fk := (a1, a2, a3, a4, a5, x) \rightarrow 1 + a1\, x^{2/3} + a2\, x^{4/3} + a3\, x^{2} + a4\, x^{8/3} + a5\, x^{10/3} - (1 + a1 + a2 + a3 + a4 + a5)\, x^{4} \tag{3}$$

```
> a:=plot(fk(-.76966093486089359,-17.6515154685407368,
  70.6109344186694160,-113.616391953257676,84.0729365812724154,x),
  x=0..1,style=point,color=red):
> b:=plot((1+(3*x)^3)*((2.7182818284590)^(-6.93*x))-x*(28/
  (2.7182818284590)^6.93),x=0..1,style=point,color=red):
> fa:=(a1,a2,a3,a4,a5,x)->1+a1*x^(1/3)+a2*x+a3*x^(5/3)+a4*x^(7/3)+
  a5*x^(9/3)-(1+a1+a2+a3+a4+a5)*x^(11/3);
```

$$fa := (a1, a2, a3, a4, a5, x) \rightarrow 1 + a1\, x^{1/3} + a2\, x + a3\, x^{5/3} + a4\, x^{7/3} + a5\, x^{3} - (1 + a1 + a2 + a3 + a4 + a5)\, x^{11/3} \tag{4}$$

```
> c:=plot(fa(-.1384712488919,-7.83711782405,20.9185449918,
  -25.0792940228,14.1484129021,x),x=0..1,style=line,color=blue):
> display(b,c);
```

Figure 6.3. Extract from Maple

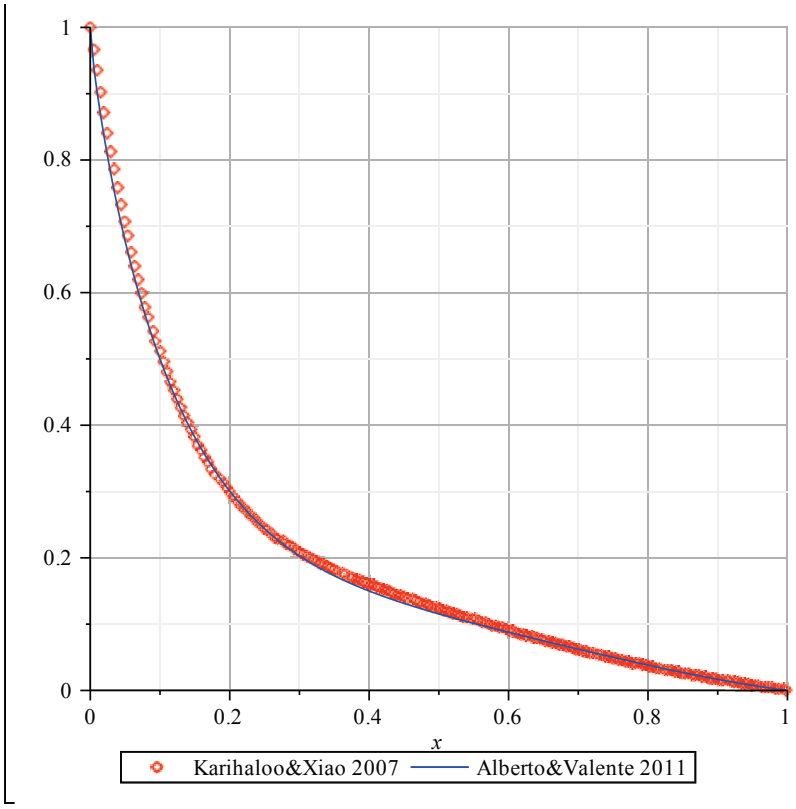

Figure 6.4. Extract from Maple

6.2 Appendix B

```
> restart;
> Digits:=16;
```

$$Digits := 16 \quad (1)$$

```
> mu:=45;
```

$$\mu := 45 \quad (2)$$

```
> E1:=24000;
```

$$E1 := 24000 \quad (3)$$

```
> E2:=41000;
```

$$E2 := 41000 \quad (4)$$

```
> ni1:=15/100;
```

$$ni1 := \frac{3}{20} \quad (5)$$

```
> ni2:=10/100;
```

$$ni2 := \frac{1}{10} \quad (6)$$

```
> r1:=240;
```

$$r1 := 240 \quad (7)$$

```
> r2:=480;
```

$$r2 := 480 \quad (8)$$

```
== N pari  2 4 6 8 10 =========
> N:=4;
```

$$N := 4 \quad (9)$$

```
=================================================================
==========================================================
> mu1:=E1/(2+2*ni1);
```

$$\mu 1 := \frac{240000}{23} \quad (10)$$

```
> mu2:=E2/(2+2*ni2);
```

$$\mu 2 := \frac{205000}{11} \quad (11)$$

```
> k1:=(3-ni1)/(1+ni1);
```

$$k1 := \frac{57}{23} \quad (12)$$

```
> k2:=(3-ni2)/(1+ni2);
```

$$k2 := \frac{29}{11} \quad (13)$$

```
> sigma1:=theta->2*lambda[n]*(a1[n]*cos((lambda[n]-1)*theta)-a2[n]*
  sin((lambda[n]-1)*theta))+lambda[n]*(lambda[n]-1)*(a1[n]*cos(
  (lambda[n]-1)*theta)-a2[n]*sin((lambda[n]-1)*theta))+(lambda[n]
  +1)*lambda[n]*(b1[n]*cos((lambda[n]-1)*theta)-b2[n]*sin((lambda
  [n]-1)*theta));
```

$$\sigma 1 := \theta \to 2\lambda_n \left(a1_n \cos\left(\left(\lambda_n - 1\right)\theta\right) - a2_n \sin\left(\left(\lambda_n - 1\right)\theta\right)\right) + \lambda_n \left(\lambda_n - 1\right)\left(a1_n \cos\left(\left(\lambda_n - 1\right)\theta\right) - a2_n \sin\left(\left(\lambda_n - 1\right)\theta\right)\right) + \left(\lambda_n + 1\right)\lambda_n \left(b1_n \cos\left(\left(\lambda_n - 1\right)\theta\right) - b2_n \sin\left(\left(\lambda_n - 1\right)\theta\right)\right) \quad (14)$$

```
> sigma2:=theta->2*lambda[n]*(g1[n]*cos((lambda[n]-1)*theta)-g2[n]*
  sin((lambda[n]-1)*theta))+lambda[n]*(lambda[n]-1)*(g1[n]*cos(
  (lambda[n]-1)*theta)-g2[n]*sin((lambda[n]-1)*theta))+(lambda[n]
  +1)*lambda[n]*(h1[n]*cos((lambda[n]-1)*theta)-h2[n]*sin((lambda
```

Figure 6.5. Extract from Maple (r=0.24 m)

```
   [n]-1)*theta));
```

$$\sigma 2 := \theta \to 2\,\lambda_n \left(g1_n \cos\left(\left(\lambda_n - 1\right)\theta\right) - g2_n \sin\left(\left(\lambda_n - 1\right)\theta\right)\right) + \lambda_n \left(\lambda_n - 1\right)\left(g1_n \cos\left(\left(\lambda_n - 1\right)\theta\right) - g2_n \sin\left(\left(\lambda_n - 1\right)\theta\right)\right) + \left(\lambda_n + 1\right)\lambda_n \left(h1_n \cos\left(\left(\lambda_n - 1\right)\theta\right) - h2_n \sin\left(\left(\lambda_n - 1\right)\theta\right)\right) \tag{15}$$

```
> sigma3:=theta->2*lambda[n]*(a1[n]*cos((lambda[n]-1)*theta)-a2[n]*
  sin((lambda[n]-1)*theta))-lambda[n]*(lambda[n]-1)*(a1[n]*cos(
  (lambda[n]-1)*theta)-a2[n]*sin((lambda[n]-1)*theta))-(lambda[n]
  +1)*lambda[n]*(b1[n]*cos((lambda[n]-1)*theta)-b2[n]*sin((lambda
  [n]-1)*theta));
```

$$\sigma 3 := \theta \to 2\,\lambda_n \left(a1_n \cos\left(\left(\lambda_n - 1\right)\theta\right) - a2_n \sin\left(\left(\lambda_n - 1\right)\theta\right)\right) - \lambda_n \left(\lambda_n - 1\right)\left(a1_n \cos\left(\left(\lambda_n - 1\right)\theta\right) - a2_n \sin\left(\left(\lambda_n - 1\right)\theta\right)\right) - \left(\lambda_n + 1\right)\lambda_n \left(b1_n \cos\left(\left(\lambda_n - 1\right)\theta\right) - b2_n \sin\left(\left(\lambda_n - 1\right)\theta\right)\right) \tag{16}$$

```
> sigma4:=theta->2*lambda[n]*(g1[n]*cos((lambda[n]-1)*theta)-g2[n]*
  sin((lambda[n]-1)*theta))-lambda[n]*(lambda[n]-1)*(g1[n]*cos(
  (lambda[n]-1)*theta)-g2[n]*sin((lambda[n]-1)*theta))-(lambda[n]
  +1)*lambda[n]*(h1[n]*cos((lambda[n]-1)*theta)-h2[n]*sin((lambda
  [n]-1)*theta));
```

$$\sigma 4 := \theta \to 2\,\lambda_n \left(g1_n \cos\left(\left(\lambda_n - 1\right)\theta\right) - g2_n \sin\left(\left(\lambda_n - 1\right)\theta\right)\right) - \lambda_n \left(\lambda_n - 1\right)\left(g1_n \cos\left(\left(\lambda_n - 1\right)\theta\right) - g2_n \sin\left(\left(\lambda_n - 1\right)\theta\right)\right) - \left(\lambda_n + 1\right)\lambda_n \left(h1_n \cos\left(\left(\lambda_n - 1\right)\theta\right) - h2_n \sin\left(\left(\lambda_n - 1\right)\theta\right)\right) \tag{17}$$

```
> tau1:=theta->lambda[n]*(lambda[n]-1)*(a1[n]*sin((lambda[n]-1)*
  theta)+a2[n]*cos((lambda[n]-1)*theta))+(lambda[n]+1)*lambda[n]*
  (b1[n]*sin((lambda[n]-1)*theta)+b2[n]*cos((lambda[n]-1)*theta));
```

$$\tau 1 := \theta \to \lambda_n \left(\lambda_n - 1\right)\left(a1_n \sin\left(\left(\lambda_n - 1\right)\theta\right) + a2_n \cos\left(\left(\lambda_n - 1\right)\theta\right)\right) + \left(\lambda_n + 1\right)\lambda_n \left(b1_n \sin\left(\left(\lambda_n - 1\right)\theta\right) + b2_n \cos\left(\left(\lambda_n - 1\right)\theta\right)\right) \tag{18}$$

```
> tau2:=theta->lambda[n]*(lambda[n]-1)*(g1[n]*sin((lambda[n]-1)*
  theta)+g2[n]*cos((lambda[n]-1)*theta))+(lambda[n]+1)*lambda[n]*
  (h1[n]*sin((lambda[n]-1)*theta)+h2[n]*cos((lambda[n]-1)*theta));
```

$$\tau 2 := \theta \to \lambda_n \left(\lambda_n - 1\right)\left(g1_n \sin\left(\left(\lambda_n - 1\right)\theta\right) + g2_n \cos\left(\left(\lambda_n - 1\right)\theta\right)\right) + \left(\lambda_n + 1\right)\lambda_n \left(h1_n \sin\left(\left(\lambda_n - 1\right)\theta\right) + h2_n \cos\left(\left(\lambda_n - 1\right)\theta\right)\right) \tag{19}$$

```
> lambda[n]:=1+n/2;
```

$$\lambda_n := 1 + \frac{1}{2}\,n \tag{20}$$

```
> sigma_y1:=unapply(sum(r^(lambda[n]-1)*sigma1(theta),n=0..N),
  theta,r):
> sigma_y2:=unapply(sum(r^(lambda[n]-1)*sigma2(theta),n=0..N),
  theta,r):
> sigma_x1:=unapply(sum(r^(lambda[n]-1)*sigma3(theta),n=0..N),
  theta,r):
> sigma_x2:=unapply(sum(r^(lambda[n]-1)*sigma4(theta),n=0..N),
  theta,r):
> tau_xy1:=unapply(sum(r^(lambda[n]-1)*tau1(theta),n=0..N),theta,r)
  :
> tau_xy2:=unapply(sum(r^(lambda[n]-1)*tau2(theta),n=0..N),theta,r)
  :
================================================================
================================================================
```

Figure 6.6. Extract from Maple (r=0.24 m)

```
> eq1:= 1/2/mu1*(k1*a1[n]-lambda[n]*a1[n]-(lambda[n]+1)*b1[n])
  -1/2/mu2*(k2*g1[n]-lambda[n]*g1[n]-(lambda[n]+1)*h1[n]);
```

$$eq1 := \frac{19}{160000}\,a1_n - \frac{23}{480000}\left(1+\frac{1}{2}n\right)a1_n - \frac{23}{480000}\left(2+\frac{1}{2}n\right)b1_n - \frac{29}{410000}\,g1_n + \frac{11}{410000}\left(1+\frac{1}{2}n\right)g1_n + \frac{11}{410000}\left(2+\frac{1}{2}n\right)h1_n \quad (21)$$

```
> eq2:= 1/2/mu1*(k1*a2[n]+lambda[n]*a2[n]+(lambda[n]+1)*b2[n])
  -1/2/mu2*(k2*g2[n]+lambda[n]*g2[n]+(lambda[n]+1)*h2[n]);
```

$$eq2 := \frac{19}{160000}\,a2_n + \frac{23}{480000}\left(1+\frac{1}{2}n\right)a2_n + \frac{23}{480000}\left(2+\frac{1}{2}n\right)b2_n - \frac{29}{410000}\,g2_n - \frac{11}{410000}\left(1+\frac{1}{2}n\right)g2_n - \frac{11}{410000}\left(2+\frac{1}{2}n\right)h2_n \quad (22)$$

```
> eq3:=2*lambda[n]*a1[n]+lambda[n]*(lambda[n]-1)*a1[n]+(lambda[n]
  +1)*lambda[n]*b1[n]-2*lambda[n]*g1[n]-lambda[n]*(lambda[n]-1)*g1
  [n]-(lambda[n]+1)*lambda[n]*h1[n];
```

$$eq3 := 2\left(1+\frac{1}{2}n\right)a1_n + \frac{1}{2}\left(1+\frac{1}{2}n\right)n\,a1_n + \left(2+\frac{1}{2}n\right)\left(1+\frac{1}{2}n\right)b1_n - 2\left(1+\frac{1}{2}n\right)g1_n - \frac{1}{2}\left(1+\frac{1}{2}n\right)n\,g1_n - \left(2+\frac{1}{2}n\right)\left(1+\frac{1}{2}n\right)h1_n \quad (23)$$

```
> eq4:= lambda[n]*(lambda[n]-1)*a2[n]+(lambda[n]+1)*lambda[n]*b2[n]
  -lambda[n]*(lambda[n]-1)*g2[n]-(lambda[n]+1)*lambda[n]*h2[n];
```

$$eq4 := \frac{1}{2}\left(1+\frac{1}{2}n\right)n\,a2_n + \left(2+\frac{1}{2}n\right)\left(1+\frac{1}{2}n\right)b2_n - \frac{1}{2}\left(1+\frac{1}{2}n\right)n\,g2_n - \left(2+\frac{1}{2}n\right)\left(1+\frac{1}{2}n\right)h2_n \quad (24)$$

```
> eq:=(g2[n]+h2[n]+mu*(a1[n]+b1[n]))*lambda[n]+(-g2[n]+h2[n]+mu*(a1
  [n]+b1[n]));
```

$$eq := \left(g2_n + h2_n + 45\,a1_n + 45\,b1_n\right)\left(1+\frac{1}{2}n\right) - g2_n + h2_n + 45\,a1_n + 45\,b1_n \quad (25)$$

```
> equ5:= -2*lambda[n]*a2[n]-lambda[n]*(lambda[n]-1)*a2[n]-(lambda
  [n]+1)*lambda[n]*b2[n]-2*lambda[n]*g2[n]-lambda[n]*(lambda[n]-1)*
  g2[n]-(lambda[n]+1)*lambda[n]*h2[n];
```

$$equ5 := -2\left(1+\frac{1}{2}n\right)a2_n - \frac{1}{2}\left(1+\frac{1}{2}n\right)n\,a2_n - \left(2+\frac{1}{2}n\right)\left(1+\frac{1}{2}n\right)b2_n - 2\left(1+\frac{1}{2}n\right)g2_n - \frac{1}{2}\left(1+\frac{1}{2}n\right)n\,g2_n - \left(2+\frac{1}{2}n\right)\left(1+\frac{1}{2}n\right)h2_n \quad (26)$$

```
> equ6:= lambda[n]*(lambda[n]-1)*a1[n]+(lambda[n]+1)*lambda[n]*b1
  [n]+lambda[n]*(lambda[n]-1)*g1[n]+(lambda[n]+1)*lambda[n]*h1[n];
```

$$equ6 := \frac{1}{2}\left(1+\frac{1}{2}n\right)n\,a1_n + \left(2+\frac{1}{2}n\right)\left(1+\frac{1}{2}n\right)b1_n + \frac{1}{2}\left(1+\frac{1}{2}n\right)n\,g1_n + \left(2+\frac{1}{2}n\right)\left(1+\frac{1}{2}n\right)h1_n \quad (27)$$

```
> equ7:= -lambda[n]*(lambda[n]-1)*g1[n]-(lambda[n]+1)*lambda[n]*h1
  [n]+mu*(-2*lambda[n]*a2[n]-lambda[n]*(lambda[n]-1)*a2[n]-(lambda
  [n]+1)*lambda[n]*b2[n]);
```

$$equ7 := -\frac{1}{2}\left(1+\frac{1}{2}n\right)n\,g1_n - \left(2+\frac{1}{2}n\right)\left(1+\frac{1}{2}n\right)h1_n - 90\left(1+\frac{1}{2}n\right)a2_n - \frac{45}{2}\left(1+\frac{1}{2}n\right)n\,a2_n - 45\left(2+\frac{1}{2}n\right)\left(1+\frac{1}{2}n\right)b2_n \quad (28)$$

Figure 6.7. Extract from Maple (r=0.24 m)

```
> n:=0;
> s0:=solve({eq1,eq2,eq3,eq4,eq},[b2[n],g1[n],g2[n],h1[n],h2[n]]);
> assign(s0);
```

$$n := 0$$

$$s0 := \left[\left[b2_0 = -45\,a1_0 - 45\,b1_0, g1_0 = \frac{245}{192}\,a1_0 - \frac{83}{192}\,b1_0, g2_0 = \frac{41}{24}\,a2_0 - \frac{1245}{64}\,a1_0 - \frac{1245}{64}\,b1_0, h1_0 = -\frac{53}{192}\,a1_0 + \frac{275}{192}\,b1_0, h2_0 = -45\,a1_0 - 45\,b1_0\right]\right] \quad (29)$$

```
> for i from 1 by 2 to N do
> n:=i:
> s1:=solve({eq1,eq2,eq3,eq4,equ5,equ6,equ7},[a2[n],b1[n],b2[n],g1
  [n],g2[n],h1[n],h2[n]]):
> assign(s1);
> n:=i+1:
> s2:=solve({eq1,eq2,eq3,eq4,eq},[b2[n],g1[n],g2[n],h1[n],h2[n]]):
> assign(s2);
> end do;
```

$$n := 1$$

$$s1 := \left[\left[a2_1 = -\frac{1}{45}\,a1_1, b1_1 = -\frac{51}{467}\,a1_1, b2_1 = \frac{283}{11675}\,a1_1, g1_1 = \frac{573}{467}\,a1_1, g2_1 = -\frac{191}{7005}\,a1_1, h1_1 = -\frac{157}{467}\,a1_1, h2_1 = \frac{2653}{105075}\,a1_1\right]\right]$$

$$n := 2$$

$$s2 := \left[\left[b2_2 = -\frac{1}{3}\,a2_2 - 45\,a1_2 - 45\,b1_2, g1_2 = \frac{407}{384}\,a1_2 - \frac{83}{128}\,b1_2, g2_2 = \frac{41}{24}\,a2_2 - \frac{3735}{128}\,a1_2 - \frac{3735}{128}\,b1_2, h1_2 = -\frac{23}{384}\,a1_2 + \frac{211}{128}\,b1_2, h2_2 = -\frac{41}{72}\,a2_2 - \frac{4515}{128}\,a1_2 - \frac{4515}{128}\,b1_2\right]\right]$$

$$n := 3$$

$$s1 := \left[\left[a2_3 = -\frac{1}{45}\,a1_3, b1_3 = -\frac{1189}{3269}\,a1_3, b2_3 = \frac{3481}{147105}\,a1_3, g1_3 = \frac{573}{467}\,a1_3, g2_3 = -\frac{191}{7005}\,a1_3, h1_3 = -\frac{1931}{3269}\,a1_3, h2_3 = \frac{3799}{147105}\,a1_3\right]\right]$$

$$n := 4$$

$$s2 := \left[\left[b2_4 = -\frac{1}{2}\,a2_4 - 45\,a1_4 - 45\,b1_4, g1_4 = \frac{27}{32}\,a1_4 - \frac{83}{96}\,b1_4, g2_4 = \frac{41}{24}\,a2_4 - \frac{1245}{32}\,a1_4 - \frac{1245}{32}\,b1_4, h1_4 = \frac{5}{32}\,a1_4 + \frac{179}{96}\,b1_4, h2_4 = -\frac{41}{48}\,a2_4 - \frac{1635}{64}\,a1_4 - \frac{1635}{64}\,b1_4\right]\right] \quad (30)$$

```
>==========================================================================
==============================================================
> #sigma_x1(theta,r);
> #sigma_x2(theta,r);
> #sigma_y1(theta,r);
> #sigma_y2(theta,r);
```

Figure 6.8. Extract from Maple (r=0.24 m)

```
> #tau_xy1(theta,r);
> #tau_xy2(theta,r);
-------------------------------------------------------
> with(linalg);
[BlockDiagonal, GramSchmidt, JordanBlock, LUdecomp, QRdecomp, Wronskian, addcol,                (31)
    addrow, adj, adjoint, angle, augment, backsub, band, basis, bezout, blockmatrix, charmat,
    charpoly, cholesky, col, coldim, colspace, colspan, companion, concat, cond, copyinto,
    crossprod, curl, definite, delcols, delrows, det, diag, diverge, dotprod, eigenvals,
    eigenvalues, eigenvectors, eigenvects, entermatrix, equal, exponential, extend, ffgausselim,
    fibonacci, forwardsub, frobenius, gausselim, gaussjord, geneqns, genmatrix, grad,
    hadamard, hermite, hessian, hilbert, htranspose, ihermite, indexfunc, innerprod, intbasis,
    inverse, ismith, issimilar, iszero, jacobian, jordan, kernel, laplacian, leastsqrs, linsolve,
    matadd, matrix, minor, minpoly, mulcol, mulrow, multiply, norm, normalize, nullspace,
    orthog, permanent, pivot, potential, randmatrix, randvector, rank, ratform, row, rowdim,
    rowspace, rowspan, rref, scalarmul, singularvals, smith, stackmatrix, submatrix, subvector,
    sumbasis, swapcol, swaprow, sylvester, toeplitz, trace, transpose, vandermonde, vecpotent,
    vectdim, vector, wronskian]
> rx1:=array(1..2*N+2):
> rx2:=array(1..2*N+2):
> ry1:=array(1..2*N+2):
> ry2:=array(1..2*N+2):
> rt1:=array(1..2*N+2):
> rt2:=array(1..2*N+2):
> rx1:=(theta,r)->[coeff(sigma_x1(theta,r),a1[0]),coeff(sigma_x1
  (theta,r),b1[0]),seq(coeff(sigma_x1(theta,r),a1[i]),i=1..N,2),seq
  (coeff(sigma_x1(theta,r),a1[i+1]),i=1..N,2),seq(coeff(sigma_x1
  (theta,r),b1[i+1]),i=1..N,2),seq(coeff(sigma_x1(theta,r),a2[i+1]
  ),i=1..N,2)]:
> rx2:=(theta,r)->[coeff(sigma_x2(theta,r),a1[0]),coeff(sigma_x2
  (theta,r),b1[0]),seq(coeff(sigma_x2(theta,r),a1[i]),i=1..N,2),seq
  (coeff(sigma_x2(theta,r),a1[i+1]),i=1..N,2),seq(coeff(sigma_x2
  (theta,r),b1[i+1]),i=1..N,2),seq(coeff(sigma_x2(theta,r),a2[i+1]
  ),i=1..N,2)]:
> ry1:=(theta,r)->[coeff(sigma_y1(theta,r),a1[0]),coeff(sigma_y1
  (theta,r),b1[0]),seq(coeff(sigma_y1(theta,r),a1[i]),i=1..N,2),seq
  (coeff(sigma_y1(theta,r),a1[i+1]),i=1..N,2),seq(coeff(sigma_y1
  (theta,r),b1[i+1]),i=1..N,2),seq(coeff(sigma_y1(theta,r),a2[i+1]
  ),i=1..N,2)]:
> ry2:=(theta,r)->[coeff(sigma_y2(theta,r),a1[0]),coeff(sigma_y2
  (theta,r),b1[0]),seq(coeff(sigma_y2(theta,r),a1[i]),i=1..N,2),seq
  (coeff(sigma_y2(theta,r),a1[i+1]),i=1..N,2),seq(coeff(sigma_y2
  (theta,r),b1[i+1]),i=1..N,2),seq(coeff(sigma_y2(theta,r),a2[i+1]
  ),i=1..N,2)]:
  rt1:=(theta,r)->[coeff(tau_xy1(theta,r),a1[0]),coeff(tau_xy1
  (theta,r),b1[0]),seq(coeff(tau_xy1(theta,r),a1[i]),i=1..N,2),seq
  (coeff(tau_xy1(theta,r),a1[i+1]),i=1..N,2),seq(coeff(tau_xy1
  (theta,r),b1[i+1]),i=1..N,2),seq(coeff(tau_xy1(theta,r),a2[i+1]),
  i=1..N,2)]:
> rt2:=(theta,r)->[coeff(tau_xy2(theta,r),a1[0]),coeff(tau_xy2
  (theta,r),b1[0]),seq(coeff(tau_xy2(theta,r),a1[i]),i=1..N,2),seq
  (coeff(tau_xy2(theta,r),a1[i+1]),i=1..N,2),seq(coeff(tau_xy2
  (theta,r),b1[i+1]),i=1..N,2),seq(coeff(tau_xy2(theta,r),a2[i+1]),
  i=1..N,2)]:

> w:=array([10e18,10e15,10e15,10e15,10e15,10e15,10e15,10e15,10e15,
  10e15,10e15,10e15,10e1,10e15,10e15,10e14,10e14,10e14,10e14,10e14,
  10e15,10e14,10e14,10e14,10e14,10e14,10e14,10e15,10e15,10e15,
```

Figure 6.9. Extract from Maple (r=0.24 m)

```
   10e14,10e14,10e14,10e14,10e14,10e14,10e14,10e18,10e15,10e15,
   10e16,10e15,10e15,10e15,10e15,10e15,10e15,10e15,10e15,10e15,
   10e15,10e16,10e14,10e14,10e14,10e14,10e14,10e15,10e15,10e15,
   10e14,10e14,10e14,10e14,10e14,10e14,10e14,10e15,10e14,10e14,
   10e14,10e14,10e14,10e14,10e14,10e14,10e14,10e14,10e14,10e15]):

> Z:=array(1..80,1..80):
> for i from 1 to 80 do
>  for j from 1 to 80 do
>  Z[i,j]:=0:
>  end do:
> end do:
> for i from 1 to 80 do
> Z[i,i]:=w[i]:
> end do:
> E:=matrix([rx2(-Pi,r1),rx2(-5*Pi/6,r1),rx2(-2*Pi/3,r1),rx2(-Pi/2,
   r1),rx2(-Pi/3,r1),rx2(-Pi/6,r1),rx2(0,r1),rx1(0,r1),rx1(Pi/6,r1),
   rx1(Pi/3,r1),rx1(Pi/2,r1),rx1(2*Pi/3,r1),rx1(5*Pi/6,r1),rx1(Pi,
   r1),ry2(-Pi,r1),ry2(-5*Pi/6,r1),ry2(-2*Pi/3,r1),ry2(-Pi/2,r1),ry2
   (-Pi/3,r1),ry2(-Pi/6,r1),ry1(0,r1),ry1(Pi/6,r1),ry1(Pi/3,r1),ry1
   (Pi/2,r1),ry1(2*Pi/3,r1),ry1(5*Pi/6,r1),ry1(Pi,r1),rt2(-Pi,r1),
   rt2(-5*Pi/6,r1),rt2(-2*Pi/3,r1),rt2(-Pi/2,r1),rt2(-Pi/3,r1),rt2(-
   Pi/6,r1),rt1(0,r1),rt1(Pi/6,r1),rt1(Pi/3,r1),rt1(Pi/2,r1),rt1(2*
   Pi/3,r1),rt1(5*Pi/6,r1),rt1(Pi,r1),rx2(-Pi,r2),rx2(-5*Pi/6,r2),
   rx2(-2*Pi/3,r2),rx2(-Pi/2,r2),rx2(-Pi/3,r2),rx2(-Pi/6,r2),rx2(0,
   r2),rx1(0,r2),rx1(Pi/6,r2),rx1(Pi/3,r2),rx1(Pi/2,r2),rx1(2*Pi/3,
   r2),rx1(5*Pi/6,r2),rx1(Pi,r2),ry2(-Pi,r2),ry2(-5*Pi/6,r2),ry2(-2*
   Pi/3,r2),ry2(-Pi/2,r2),ry2(-Pi/3,r2),ry2(-Pi/6,r2),ry1(0,r2),ry1
   (Pi/6,r2),ry1(Pi/3,r2),ry1(Pi/2,r2),ry1(2*Pi/3,r2),ry1(5*Pi/6,
   r2),ry1(Pi,r2),rt2(-Pi,r2),rt2(-5*Pi/6,r2),rt2(-2*Pi/3,r2),rt2(-
   Pi/2,r2),rt2(-Pi/3,r2),rt2(-Pi/6,r2),rt1(0,r2),rt1(Pi/6,r2),rt1
   (Pi/3,r2),rt1(Pi/2,r2),rt1(2*Pi/3,r2),rt1(5*Pi/6,r2),rt1(Pi,r2)])
   :

> A:=evalm(Z&*E):
> AT:=transpose(A):
> ATA:=evalf(evalm(AT&*A)):
> #det(ATA):
> evalf(det(ATA));
                          7.487903356551105 10^426                    (32)

> C:=inverse(ATA):

> #B:=evalf(evalm(C&*ATA));
> u:=transpose(matrix([[1.36e6,1.14e6,1.05e6,9.67e5,8.77e5,8.62e5,
   7.93e5,3.83e5,3.60e5,2.70e5,2.44e5,2.12e5,2.67e5,2.93e5,1.15e4,
   3.74e3,-3.31e4,-9.14e4,-1.56e5,-1.75e5,-1.78e5,-1.31e5,-8.31e4,
   -3.65e4,-6.11e3,1.03e4,1.23e4,8.02e5,7.61e5,6.77e5,6.55e5,6.45e5,
   6.99e5,7.37e5,7.74e5,7.74e5,7.77e5,7.69e5,7.96e5,8.09e5,1.55e6,
   1.31e6,1.16e6,1.03e6,9.43e5,8.05e5,6.82e5,3.42e5,1.85e5,6.73e4,
   -1.62e4,-6.62e4,-6.01e4,-4.27e4,2.33e4,2.45e4,-2.41e4,-1.40e5,
   -2.45e5,-2.72e5,-2.38e5,-1.66e5,-9.53e4,-3.25e4,-8.78e3,2.52e3,
   1.14e4,9.22e5,8.15e5,6.72e5,6.15e5,6.32e5,7.19e5,7.73e5,8.20e5,
   8.13e5,7.87e5,7.85e5,8.44e5,9.22e5]])):
> q:=evalm(Z&*u):
> v:=evalm(AT&*q):
> R:=evalf(evalm(C&*v)):
> a1[0]:=R[1,1];
```

Figure 6.10. Extract from Maple (r=0.24 m)

$$a1_0 := 1.71092385706\ 10^5 \quad (33)$$

```
> b1[0]:=R[2,1];
```

$$b1_0 := -1.79457501070\ 10^5 \quad (34)$$

```
> for i from 1 by 2 to N do
> n:=i:
> a1[n]:=R[2+(n+1)/2,1]:
> a1[n+1]:=R[2+(n+1)/2+N/2,1]:
> b1[n+1]:=R[2+(n+1)/2+N,1]:
> a2[n+1]:=R[2+(n+1)/2+3*N/2,1]:
> end do;
```

$$n := 1$$
$$a1_1 := -7214.1065110$$
$$a1_2 := -36.040486173$$
$$b1_2 := 36.908129290$$
$$a2_2 := 128.241434280$$
$$n := 3$$
$$a1_3 := 4.2510030572$$
$$a1_4 := 0.014289106016$$
$$b1_4 := -0.014839954832$$
$$a2_4 := -0.015400804553 \quad (35)$$

```
> sigma_x1(theta,r);
```

$$7.01099773552\ 10^5 + \sqrt{r}\left(-19186.12481083940\cos\left(\frac{1}{2}\theta\right) - 1016.462973070235\sin\left(\frac{1}{2}\theta\right)\right) + r\left(-293.529748086\cos(\theta) - 747.229378710000\sin(\theta)\right) + r^{3/2}\left(18.84277586382013\cos\left(\frac{3}{2}\theta\right) + 0.9982726665373308\sin\left(\frac{3}{2}\theta\right)\right) + r^2\left(0.178079457984\cos(2\theta) + 0.3898631879580000\sin(2\theta)\right) \quad (36)$$

```
> #sigma_x2(theta,r);
> #sigma_y1(theta,r);
> #sigma_y2(theta,r);
> #tau_xy1(theta,r);
> #tau_xy2(theta,r);
> with(plots);
```

[*animate*, *animate3d*, *animatecurve*, *arrow*, *changecoords*, *complexplot*, *complexplot3d*, *conformal*, *conformal3d*, *contourplot*, *contourplot3d*, *coordplot*, *coordplot3d*, *densityplot*, *display*, *dualaxisplot*, *fieldplot*, *fieldplot3d*, *gradplot*, *gradplot3d*, *implicitplot*, *implicitplot3d*, *inequal*, *interactive*, *interactiveparams*, *intersectplot*, *listcontplot*, *listcontplot3d*, *listdensityplot*, *listplot*, *listplot3d*, *loglogplot*, *logplot*, *matrixplot*, *multiple*, *odeplot*, *pareto*, *plotcompare*, *pointplot*, *pointplot3d*, *polarplot*, *polygonplot*, *polygonplot3d*, *polyhedra_supported*, *polyhedraplot*, *rootlocus*, *semilogplot*, *setcolors*, *setoptions*, *setoptions3d*, *spacecurve*, *sparsematrixplot*, *surfdata*, *textplot*, *textplot3d*, *tubeplot*] (37)

Figure 6.11. Extract from Maple (r=0.24 m)

```
> a:=plot(sigma_x1(t,r2),t=0..Pi,style=line,color=blue):
> b:=plot(sigma_y1(t,r2),t=0..Pi,style=line,color=red):
> c:=plot(tau_xy1(t,r2),t=0..Pi,style=line,color=black):
> d:=plot(sigma_x2(t,r2),t=-Pi..0,style=line,color=blue):
> e:=plot(sigma_y2(t,r2),t=-Pi..0,style=line,color=red):
> f:=plot(tau_xy2(t,r2),t=-Pi..0,style=line,color=black):
> p1:=display(a,d):
> p2:=display(b,e):
> p3:=display(c,f):
> u0:=<-Pi,-5*Pi/6,-4*Pi/6,-Pi/2,-Pi/3,-Pi/6,0,0,Pi/6,Pi/3,Pi/2,2*
  Pi/3,5*Pi/6,Pi>:
> uu:=<-Pi,-5*Pi/6,-4*Pi/6,-Pi/2,-Pi/3,-Pi/6,0,Pi/6,Pi/3,Pi/2,2*
  Pi/3,5*Pi/6,Pi>:
> u1:=<1.55e6,1.31e6,1.16e6,1.03e6,9.43e5,8.05e5,6.82e5,3.42e5,
  1.85e5,6.73e4,-1.62e4,-6.62e4,-6.01e4,-4.27e4>:
> u2:=<2.33e4,2.45e4,-2.41e4,-1.40e5,-2.45e5,-2.72e5,-2.38e5,
  -1.66e5,-9.53e4,-3.25e4,-8.78e3,2.52e3,1.14e4>:
> u3:=<9.22e5,8.15e5,6.72e5,6.15e5,6.32e5,7.19e5,7.73e5,8.20e5,
  8.13e5,7.87e5,7.85e5,8.44e5,9.22e5>:
> g1:=plot(u0, u1, color=blue, symbol=circle,style=point):
> g2:=plot(uu, u2, color=red, symbol=circle,style=point):
> g3:=plot(uu, u3, color=black, symbol=circle, style=point):
> q1:=display(g1):
> q2:=display(g2):
> q3:=display(g3):
> display(p1,p2,p3,q1,q2,q3);
```

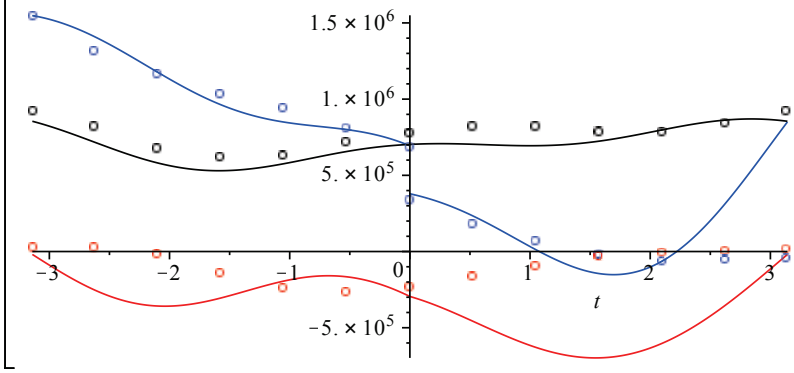

Figure 6.12. Extract from Maple (r=0.24 m)

Similarly, in the case $r = 0.48\ m$, we obtain:

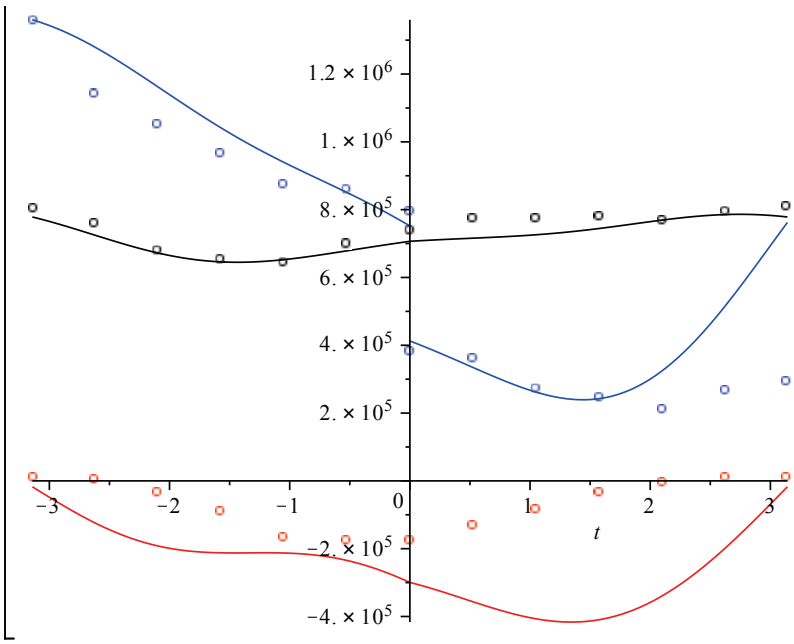

Figure 6.13. Extract from Maple (r=0.48 m)

Chapter 7

List of symbols

- $'$: derivative with respect to z
- a_{1n},a_{2n},b_{1n},b_{2n}: real coefficients
- $A_n = a_{1n} + ia_{2n}$,$B_n = b_{1n} + ib_{2n}$: complex coefficients
- α_1,α_2,... : best fitting constants
- c: joint cohesion
- E: Young modulus
- ν: Poisson's ratio
- δ: crack sliding displacement (CSD)
- δ_c: critical value of δ
- f_t: ultimate tensile strength
- h_{iff} : imminent failure flood water level
- $h_{ovt} = h_{iff} - h_c$: over-topping water heigth
- h_c: dam crest height
- i: imaginary unit, iteration number

- K_1: mode I stress intensity factor
- K_2: mode II stress intensity factor
- λ_i: eigenvalues
- k: Kolosov constant
- $\mu = E/(2(1+\nu))$: shear modulus
- μ_f: coefficient of kinetic friction
- $\phi_1(z)$,$\chi_1(z)$: analytic functions
- r: polar coordinate
- σ_x: stress along x direction
- σ_y: stress along y direction
- σ_c: critical value of σ_y (corresponding to $w = 0$)
- $(\sigma_0$,$\mu_f\sigma_0)$: failure envelope
- τ_{xy}: tangential stress
- θ : polar coordinate
- u: displacement along x
- v: displacement along y
- w: crack opening displacement (COD)
- w_c: critical value of w
- $w_{eff} = \sqrt{w^2 + \delta^2}$: effective joint opening
- $w_{eff,c}$: critical value of w_{eff}
- $z = re^{i\theta}$: complex variable

Bibliography

[1] A. Carpinteri Mechanical Damage and Crack Growth in Concrete. *Martinus Nijhoff*, Dordrecht (The Netherlands), 1886.

[2] A. Carpinteri. Size effects on strength, toughness and ductility. *Journal of Mechanics and Physics of Solids*,pages 567-582, volume 37,1989.

[3] A. Carpinteri. Cusp catastrophe interpretation of softening instability. *Journal of Engineering Mechanics (ASCE)*,pages 1375-1392, volume 115,1989.

[4] Kirsh G. Die Theorie der elastisizat und die Bed§rfnisse der festigkeitslehre. *Zeitschrift des Vereins Deutscher Ingenieure*, Vol.42 pages 797-807, 1898.

[5] Inglis C.E. Stresses in a plate due to the presence of cracks and sharp corners. *Transaction of the Royal Institution of Naval Architect* , Vol. 60, pages 163-198 , 1921.

[6] Griffith A.A. The phenomena of rupture and flow in solids. *Philosophical Transaction of the Royal Society* , Londra, A221 pp. 219-241, 1913.

[7] Griffith A.A. The theory of rupture. *Proceedings of the First International Congress of Applied Mechanics* (Biezeno and Burgers ads.),Waltman, Londra, pp. 55-63 , 1924.

[8] Carpinteri A. Crack dominate e microcracks nei materiali fragili. *Giornale del genio Civile* , 1-2-3 , pp. 67-82 , 1978.

[9] Irwin G. R. Analysis of stresses and strains near the end of the crack traversing a plate. *Journal of applied Mechanics* ,Vol. 24, pp. 361 - 364, 1957.

[10] Westergaard H. M. Bearing pressure and cracks. *Journal of applied Mechanics* ,Vol. 6, pp. 49-53, 1939.

[11] Sih G. C. Handbook of Stress Intensity Factors. Lehigh University, Bethlehm , 1973.

[12] Tada H., Paris P.C., Irwin G.R. Stress Analysis of Cracks Handbook. Del Research Corporation, Hellerttown , 1973.

[13] Rooke D.R., Cartwright D.J. Compendium of Stress Intensity Factors. Hellingdon Press,Uxbridge , 1976.

[14] Murakami Y. Stress Intensity Factors Handbook. Vol.I-II,Pergamon Press, Oxford, 1987.

[15] Carpinteri A. Meccanica dei Materiali e della Frattura Pitagora, Bologna, 1992.

[16] Irwin G. R. Plastic zone near a crack and fracture toughness. *Proceedings of the 7th Sagamore Conference* ,IV-63, 1960.

[17] Rice J. R. A path indipendent integral and the approximate analysis of strain concentrations by notches and cracks. *Journal of Applied Mechanics* ,Vol. 35,pp. 379-386, 1968.

[18] Carpinteri A. Notch sensitivity in fracture testing of aggregative materials. *Engineering Fracture Mechanics* ,Vol. 16,pp. 467-481, 1982.

[19] Barenblatt G. I. The formation of equilibrium cracks during brittle fracture:general ideas and hypotheses. Axially-simmetric cracks. *Journal of Applied Mathematics and Mechanics* ,Vol. 23,pp. 622-636, 1959.

[20] Dugdale D. S. Yielding of steel sheets containing slits. *Journal of Mechanics and Physics of Solid* ,Vol. 8,pp. 100-104, 1960.

[21] Barenblatt G. I. The mathematical theory of equilibrium cracks in brittle fracture. *Advance in Applied Mechanics* ,Vol. 7,pp. 52-129, 1962.

[22] Carpinteri A. Interpretation of the Griffith instability as a bifurcation of global equilibrium. *N.A.T.O. Advanced Research Workshop on Application of Fracture Mechanics to Cementitious Composites (S.P. Shah ed.)* ,Evanston (Illinois), 4-7 Settembre 1984, Martinus Nijhoff, pp. 287-316,1984.

[23] Carpinteri A. Size scale effects on the brittleness of concrete structures:dimensional analysis and snap-back instability. *America Concrete Institute* ,ACI SP-118 (V.Li,Z.P. Bazant eds.) ,Detroit, pp. 197-235,1989.

[24] Hillerborg A.,Modeer M.,Peterson P.E. Analysis of crack formation and crack growth in concrete by means of fracture mechanics and finite elements. *Cement and Concrete Research* ,Vol. 6,pp. 773-782, 1976.

[25] Irwin G. R. Fracture Testing of high strength sheet material *A.S.T.M. Bullettin* ,pp. 29, 1960.

[26] Bilby B.A.,Cottrell A.H.,Swinden K.H. The spread of plastic yield from a notch. *Proceedings of the Royal Society* 1A272,pp. 151-162, 1967.

[27] Willis J.R. A comparison of the fracture criteria of Griffith and Barenblatt. *Journal of Mechanics and Physics of Solid* Vol.15,pp. 151-162, 1967.

[28] Wnuk M.P. Quasi-static extension of a tensile crack contained in a viscoelastic-plastic solid. *Journal of Applied Mechanics* Vol.41,pp. 234-242, 1974.

[29] Carpinteri A.,Di Tommaso A.,Fanelli M. Influence of material parameters and geometry on cohesive crack propagation. *Fracture Toughness and Fracture Energy of Concrete* (F.H.Wittman ed.), Elsevier Science Publisher,pp.117-135, 1985.

[30] Carpinteri A.,Di Tommaso A.,Ferrara G.,Melchiorri G. Experimental evaluation of concrete fracture energy through a new identification method. *Fracture Toughness and Fracture Energy of Concrete* (F.H.Wittman ed.), Elsevier Science Publisher,pp.423-436, 1985

[31] Ferro G. Effetti di scala sulla resistenza a trazione dei materiali. *Tesi di Dottorato,Dipartimento di Ingegneria Strutturale,Politecnico di Torino* , 1994.

[32] Chiaia B. Influenza del Disordine Microstrutturale sulle ProprietĹ Meccaniche dei materiali Eterogenei. *Tesi di Dottorato,Dipartimento di Ingegneria Strutturale,Politecnico di Torino* , 1995.

[33] Colombo G.,Limido E. A numerical method for the analysis of stable

TPBT test:comparison with some experimental data. XI Convegno Nazionale per l'Analisi delle sollecitazioni,Torino,pp.233-243,1983.

[34] Carpinteri A.,Colombo G. Numerical analysis of catastrophic softening behavior (snap-back instability). *Computers and Structures* Vol.31,pp. 607-636, 1989.

[35] Li Y.N.,Liang R.Y. Stability theory of cohesive crack model. *Journal of Engineering Mechanics* Vol.118,No.3,pp. 587-603, 1992.

[36] Li Y.N.,Liang R.Y. The theory of boundary eigenvalue problem in the cohesive crack model and its application. *Journal of Mechanics and Physics Solid* Vol.41,No.2,pp.331-350, 1993.

[37] Carpinteri A.,Valente S. Numerical modeling of mixed mode cohesive crack propagation. *International Conferences on Computational Engineering Science(S.N.Alturi,G.Yagawa eds.)* 10-18 Aprile 1988,Atlanta (Georgia),pp.12.vi.1-12.vi.2, 1988.

[38] Carpinteri A.,Valente S. Size scale transition from ductile to brittle fracture:a dimensional analysis approach. *Proceedings of the France-U.S. Workshop on Strain - Localisation and Size-Effect due to Cracking and Damage* Elsevier Applied Science,pp.477-490, 1988.

[39] Lawson C.L.,Hanson R.J. Solving Least Squares Problems. Prentice-Hall Inc.Englewood Cliffs,New-Jersey,1974.

[40] Valente S. Bifurcation phenomena in cohesive crack propagation. *Computers and Structures* Vol.44,No.1/2,pp. 52-62, 1992.

[41] J. Červenka, J.M.Chandra Kishen, and V.E. Saouma. Mixed mode fracture of cementitious bimaterial interfaces; part ii: Numerical simulations. *Engineering Fracture Mechanics*, 60(1):95–107, 1998.

[42] F. Barpi and S. Valente. The cohesive frictional crack model applied to the analysis of the dam-foundation joint. *Engineering Fracture Mechanics*, pages 2182–2191, 2010. ISSN: 0013-7944, doi: 10.1016/j.engfracmech.2010.02.030.

[43] Bocca P., Grazzini A. Experimental procedure for the pre-qualification of strengthneing mortars. *International Journal of Architectural Heritage*,6(3): 302-321,2012.

[44] Grazzini A. Experimental techniques for the evaluation of the durability of strengthening works on historical masonry. *Masonry International* ,2006,19: 113-126.

[45] Dassault System Simulia Corp., Providence, RI, ABAQUS, release 6.10, 2010.

[46] Barpi F. ,Valente S. Size-effects induced bifurcation phenomena during multiple cohesive crack propagation. *International Journal of Solids and Structures* ,1998, 35(16):1851-1861.

[47] Barpi F. ,Valente S. Modeling water penetration at dam-foundation joint. *Engineering Fracture Mechanics*,2008,75/3-4:629-642; 10.1016/ j.engfracmech.2007.02.008.

[48] B. L. Karihaloo Fracture Mechanics and Structural Concrete. *Longman Scientific and Technical*, England, 1995.

[49] R. De Borst and M.A. Gutierrez and G.N. Wells and J.J.C. Remmers Cohesive-zone models, higher-order continuum theories and reliability methods for computational failure mechanics. *International Journal of Numerical Methods in Engineering*,Vol.60, pages 289-315, 2004.

[50] N. Moes and J.Dolbow and T. Belytschko A finite element method for crack growth without remeshing. *International Journal of Numerical Methods in Engineering*,Vol.46, pages 131-150, 1999.

[51] T. Strouboulis and K. Copps and I. Babuska The generalized finite element method. *Computer Methods in Applied Mechanics and Engineering*,Vol.190, pages 4081-4193, 2001.

[52] B.L. Karihaloo and Q.Z. Xiao Modelling of stationary and growing cracks in finite element framework without remeshing: a state-of-the-art review. *Computers and Structures*,Vol.81, pages 119-129, 2003.

[53] G. Zi and T. Belytschko New crack-tip elements for XFEM and applications to cohesive crack. *International Journal of Numerical Methods in Engineering*,Vol.57, pages 2221-2240, 2003.

[54] J. Alfaiate and A. Simone and L.J. Sluys Non-homogeneous displacement jumps in strong embedded discontinuities. *International Journal of Solids and Structures*,Vol.40, pages 5799-5817, 2003.

[55] S. Mariani and U. Perego Extended finite element method for quasi-brittle fracture. *International Journal of Numerical Methods in Engineering* 2003,pages 103-126, volume 58.

[56] B.L. Karihaloo and Q.Z. Xiao. Asymptotic fields at the tip of a cohesive crack. *International Journal of Fracture*, 150:55–74, 2008.

[57] W.Zhang and X.Deng Asymptotic fields around an interfacial crack with a cohesive zone ahead of the crack tip. *International Journal of Solids and Structures*,Vol.43, pages 2989-3005, 2006.

[58] S. Valente Influence of friction on cohesive crack propagation. *RILEM/ESIS Conf.on Fracture Processes in Concrete Rock and Ceramics*, J. G. M. van Mier and J. G. Rots and A. Bakker,E&FN Spon, pages 695-704, 1991.

[59] G. Cocchetti and G. Maier and X. Shen Piecewise linear models for interfaces and mixed mode cohesive cracks. *Journal of Engineering Mechanics (ASCE)*,Vol.3, pages 279-298, 2002.

[60] ICOLD. Imminent failure flood for a concrete gravity dam. In *5th International Benchmark Workshop on Numerical Analysis of Dams*, Denver,CO, 1999.

[61] G. Bolzon and G. Cocchetti Direct assessment of structural resistence against pressurized fracture. *International Journal for Numerical and Analytical Methods in Geomechanics* 2003, pages 353-378, volume 27.

[62] F. Barpi Numerical Models for the Study of Cracking Phenomena in Dams. *Tesi di Dottorato,Dipartimento di Ingegneria Strutturale,Politecnico di Torino* , 1996.

[63] P. Manfredini Finite element analysis of crack propagation and of plastic collapse for safety assessment of gravity concrete dam. *Tesi di Dottorato,Dipartimento di Ingegneria Strutturale,Politecnico di Milano* , 2000.

[64] E. Puntel Experimental and numerical investigation of the monotonic and cyclic behaviour of concrete dam joints. *Tesi di Dottorato,Dipartimento di Ingegneria Strutturale,Politecnico di Milano* , 2004.

[65] M.L.Williams. The stresses around a fault or crack in dissimilar media.

Bull. Seismological Soc.America 49, 199 to 404 (1959).

[66] B.M.Malyshev and R.L.Salganik The strenght of adhesive joint using the theory of fracture. *Int.J.Fracture Mech.* 1, 114 to 128 (1965).

[67] M. Hassanzadeh Behaviour of fracture process zone in concrete influenced by simultaneously applied normal and shear displacements. *Lund Institue of Technology, Sweden*, 1991.

[68] G.C. Sih and H. Liebowitz. Mathematical theories of brittle fracture. In H. Liebowitz, editor, *Fracture (vol. II)*, pages 67–190. Academic Press (New York), 1968.

[69] Alberto A., Barpi F., Valente S. Asymptotic fields at the tip of a cohesive crack growing at bi-material interface Proceedings of XX AIMETA Conference, Bologna, Italy,MEM-166-0.pdf on CD, 2011.

[70] W. Reich and E. Brühwiler and V. Slowik and V.E. Saouma Experimental and computational aspects of a water/fracture interaction. *E. Bourdarot and J. Mazars and V. Saouma*, Balkema, pages 123-131, 1994.

[71] www.3ds.com Abaqus release 6.8 *Dassault System Simulia Corp*,Providence,RI,USA, 2008.

[72] B.L. Karihaloo and Q.Z. Xiao. Accurate simulation of frictionless and frictional cohesive crack growth in quasi-brittle materials using xfem. In A. Carpinteri, P. Gambarova, G. Ferro, and G. Plizzari, editors, *Sixth International Conference on Fracture Mechanics of Concrete and Concrete Structures (FRAMCOS6)*, pages 99–110. Taylor and Francis (London), 2007.

[73] F. Barpi and S. Valente. The cohesive frictional crack model applied to the analysis of the dam-foundation joint. *Engineering Fracture Mechanics*, pages 2182–2191, 2010. ISSN: 0013-7944, doi: 10.1016/j.engfracmech.2010.02.030.

[74] Bocca P., Grazzini A., Masera D., Alberto A.,Valente S. Mechanical interaction between historical brick and repair mortar: experimental and numerical tests. *Journal of Physics* ,2011 vol. 305 n. 1. ISSN 1742-6588.

[75] Alberto A.,Antonaci P.,Valente S. Damage analysis of brick-to-mortar

interfaces. *11th International Conference on the Mechanical Behavior of Materials*2011,Como (Italy) pp. 1151-1156.

[76] Alberto A.,Valente S. Mixed mode cohesive crack growth at the bi-material interface between a dam and foundation rock. *4^{th} International Conference on Crack Paths* 2012,Gaeta,ISBN:9788895940441,ISSN:2281-1060 .

[77] Alberto A., Barpi F., Valente S. Cohesive frictional crack at bi-material interface. *II International Conference on Computational Modeling of Fracture and Failure of Materials and Structures* ,6-8 Giugno 2011,Barcellona,pag.138

[78] P. Bocca and S. Valente and A. Grazzini and A. Alberto Delamination of dehumidified repair mortars: a new experimental and numerical analysis. *Proceedings of 8th Int.Conf. on Structural Analysis of Historical Constructions, Wroclaw, Poland*,Jerzi Jasienko ,DWE, pages 628–636, ISBN: 9788371252174, 2012.